Validating the Use of Boron Nanoparticles to Quantify Tumor Oxygen Tension in Irradiated Breast Tumors

by

Li Ting Chan

Graduate Program in Medical Physics
Duke Kunshan and Duke University

Date:_____

Approved:

_____
Gregory M. Palmer, Supervisor

_____
Mark W. Dewhirst

_____
Fang-Fang Yin

Thesis submitted in partial fulfillment of
the requirements for the degree of Master of Science in the
Graduate Program in Medical Physics
in the Graduate School
of Duke Kunshan and Duke University

2019

ABSTRACT

Validating the Use of Boron Nanoparticles to Quantify Tumor Oxygen Tension in Irradiated Breast Tumors

by

Li Ting Chan

Graduate Program in Medical Physics
Duke Kunshan and Duke University

Date:_____

Approved:

_____
Gregory M. Palmer, Supervisor

_____
Mark W. Dewhirst

_____
Fang-Fang Yin

An abstract of a thesis submitted in partial
fulfillment of the requirements for the degree
of Master of Science in the
Graduate Program in Medical Physics
in the Graduate School of
Duke Kunshan and Duke University

2019

Abstract

Although hypoxia in tumors has long been identified as a key contributor to poor patient outcome, clinical solutions to lessen its deleterious effects have not been forthcoming. One reason is that there have been few means to directly quantify hypoxia kinetics with adequate spatial and temporal resolution. Dual-emissive boron nanoparticles show promise in this regard. Fluorescence imaging of these dual-emissive boron nanoparticles allows quantification of oxygen tension in a tumor microenvironment; this is accomplished by calculating the ratio of oxygen-independent fluorescence signal to oxygen-dependent phosphorescence signal.

In this work, we demonstrate the ability of these nanoparticles to, in conjunction with hyperspectral imaging of hemoglobin saturation, quantitatively characterize the oxygenation state of irradiated murine tumors *in vivo.* Mice were implanted with E0771 tumors in dorsal window chambers, and tumors were irradiated with 12Gy. Fluorescence images of dual-emissive nanoparticles injected into the tumors, as well as hyperspectral images of hemoglobin saturation, were obtained 1 day before irradiation and 2 days after irradiation. 2-way ANOVA statistical analysis revealed that while oxygen supply to the tumors – indicated by hemoglobin saturation – did not change significantly after irradiation, fluorescence-to-phosphorescence ratios – which indicate oxygen tension in the tumor – increased significantly post-irradiation. Through its

success in demonstrating radiation-induced reoxygenation in E0771 tumors, the nanoparticles show promise for further applications in characterizing oxygenation states of various tumors post-treatment. This finding also further underscores the importance of using direct techniques in quantitative studies of tumor oxygen tension.

This work presents a second technological objective: to determine if folic acid-conjugated nanoparticles can successfully target folate receptor-expressing cell lines. This is a key step towards more practical delivery of the nanoparticles to deep tumor tissue via intravenous administration, as well as to enable intracellular quantification of oxygen tension. MDA-MB-231 cells were incubated overnight with varying concentrations of folic acid-conjugated nanoparticles. Fluorescence images were obtained to determine uptake of nanoparticles. The results have been encouraging; nanoparticle internalization was observed in almost all cells at all tested concentrations, and higher concentrations of nanoparticles appeared to increase the amounts of nanoparticles internalized per cell.

This work has validated that dual-emissive boron nanoparticles can directly quantify tumor oxygen tension post-irradiation, and that folic acid-conjugated boron nanoparticles can successfully target folate receptor-overexpressing cells. Hence, the immediate next step is to introduce folate receptor-targeting abilities to dual-emissive nanoparticles for improved performance in tumor oxygen-sensing applications.

Contents

List of Tables

List of Figures

Acknowledgements

I am indebted to Dr. Gregory Palmer, my advisor, who granted me the invaluable opportunity to work with him and his lab members. Because of his patience I became less afraid of failure, and yet it was also because of his persistence that this work came to be what it is today. I am incredibly grateful for his gentle guidance and encouragement throughout the course of the thesis project.

I would also like to extend my gratitude to my two other committee members, Dr. Mark Dewhirst and Dr. Fang-Fang Yin. I am much obliged to Dr. Dewhirst who many a time pointed me towards papers that helped better my understanding of hypoxia, and who also granted me permission to use one of his figures.

The faculty at Duke Kunshan have also been extremely supportive of my research ventures. Dr. James Bowsher periodically checked in on my research progress and also offered me general advice whenever I was stuck in a rut. My thanks also extend to Dr. David Huang, who spared me his time to help me practice my defense even though he was not part of my thesis committee.

The experiments described in Chapter 2 were carried out by Dr. Hengtao Zhang. I am grateful for the support he had provided me while I was analyzing his data.

This work could not have been completed without Ashlyn Rickard, who took me under her wing from the first week I stepped into the Palmer lab. Thank you for always

taking the time out to salvage my experiments and answer my numerous questions, even when they were for class and unrelated to research! Thank you for also being my biggest cheerleader, and for tirelessly providing timely critique to all my endeavors.

Thanks also to Kenneth Young, who taught me nearly everything I needed to know about biological research, and who also drilled into me the importance of conscientious and ethical scientific research. Thank you also for always making sure that I had everything I needed during my stay in Durham!

To the rest of the members of the Palmer lab, thank you for warmly welcoming me to the lab! Special mentions to: Stefan Stryker, whose expertise with spectral component separation and MATLAB greatly contributed to this work; Jonah Orr, who always readily provided clinical insights into the various research activities at the lab and also helped me practice my defense; and Dianne Young, who was always on the ball whenever I needed help with lab administrative matters. Thanks also to Dr. David Alcorta from down the corridor, who graciously helped me with the Western Blots.

A final thanks to my peers and the administrative staff at Duke Kunshan for the camaraderie throughout the two years, and for the moral support offered during the writing of this thesis! Claire Luo took on the heavy burden of ensuring that I met all the administrative requirements at Duke Kunshan for graduation, and I am hopeful that her efforts were not in vain.

Soli Deo Gloria.

1 Introduction

Hypoxia in tumor microenvironments, defined when the partial pressure of oxygen (pO_2) falls below 10 mmHg, has been correlated with as much as a threefold increase in resistance to radiation therapies.[1] Hypoxia can be chronic or cyclic – it is chronic when the microenvironment has persistently low pO_2 levels, and is cyclic when pO_2 levels undergo periodic fluctuations that can vary as much as 20 mmHg.[2] Current techniques like *in vivo* PET and MR imaging, as well as *ex vivo* immunohistochemistry, have been able to determine the presence of chronic hypoxia, but with significant limitations: most existing methods are incapable of directly quantifying pO_2 in the microenvironment without perturbing it, which in turn affects repeatability, and/or are lacking in temporal and spatial resolution for precise and accurate measurements. As a result, the problem of hypoxia-induced tumor radio-resistance has been challenging to address clinically.

Due to their perceived potential in overcoming current limits on spatial and temporal resolution, nanoparticles have recently garnered interest in hypoxia imaging. The Palmer Lab at Duke University, in collaboration with the Fraser Lab at the University of Virginia, has pioneered a dual-emissive oxygen-sensing boron nanoparticle. Previous studies have demonstrated its utility in quantifying pO_2 *in vitro* and *in vivo*.[3] This thesis presents work that extends the applicability of these boron nanoparticles by: 1) testing its sensitivity in quantifying radiation-induced changes in

tumor oxygen concentration *in vivo*, and; 2) testing the effectiveness of conjugating the nanoparticle with folic acid to enhance nanoparticle uptake in folate-receptor expressing cells.

The remainder of this chapter discusses key concepts relevant to this work in further detail. Chapter 2 reports the results of using oxygen-sensing boron nanoparticles to track radiation-induced changes in the oxygenation of irradiated mice tumors *in vivo*. Chapter 3 presents the results of using boron nanoparticles conjugated with folic acid to target MDA-MB-231 breast cancer cells *in vitro*. These chapters are then followed by a discussion on the implications of the results of the entire work.

1.1 Hypoxia

The oxygenation state of a tissue is dependent on the balance between oxygen supply and demand, and hypoxia arises when there is an imbalance between these two factors.[4] Dewhirst *et al.* highlights eight dominant features of hypoxic tumors: 1) arteriolar supply is relatively sparse; 2) microvessels in the area are inefficiently orientated; 3) vascular density is low; 4) red blood cell flux in microvessels vary significantly; 5) oxygen gradients exist between areas nearer the arteriolar network and those further away; 6) red blood cells that are hypoxic become stiff, which further exacerbates hypoxia by causing sluggish red blood

flow; 7) existence of large diameter shunts that divert blood flow away from an area, and; 8) existence of cyclical hypoxia.[5]

Hypoxic conditions trigger hypoxia-inducible factor-1 (HIF-1) signaling, and this in turn prompts many other genetic transcriptional changes.[6] One of these is the transcription of the vascular endothelial growth factor (VEGF) which stimulates blood vessel growth in tumors.[4,6] Unlike angiogenesis in normal tissues where vessels are fully-formed and well-organized to deliver a steady and sufficient supply of oxygen, vascular growth in tumors tends to be extremely chaotic and poorly-formed.[7] These poorly-formed vessels are often leaky – this leakiness allows tumor cells to penetrate and enter the circulatory system, leading to metastasis.[8]

The chaotic formation of vessels in tumors also affects the nature of hypoxia in these cells. Chronic hypoxia typically arises when cells are located far away from oxygen-delivering blood vessels.[9] Given the inefficient formation of vessels, some cancer cells are located further away from blood vessels than the oxygen diffusion distance. The oxygen diffusion distance is on the order of $100\mu m$; any further away from blood vessels means that the cells risk having an insufficient oxygen supply in the long term.[10] Such cells are thus in a chronic state of hypoxia.

Cycling hypoxia, on the other hand, describes cells that experience cyclical fluctuations in pO_2 in their microenvironments.[9] Cycling hypoxia is believed to be the result of either changes in oxygen delivery or changes in oxygen consumption, or both.[4] The former has been more extensively studied – red cell flux has been demonstrated to correlate with tissue pO_2.[4] Chaotic and poorly-regulated vessel formation in tumors also often results in perfusion inefficiencies that adversely affect oxygen delivery.[5] Occlusions and shunts are more common in tumors; these features can cause variation in perfusion, which in turn can lead to cycling hypoxia. This suggests a temporal instability in hypoxia conditions – places that were previously normoxic can turn hypoxic.

Dewhirst had previously described both forms of hypoxia in terms of high and low tides around a low-lying island, as illustrated in Figure 1.1.[4] At high tide, the entire island may be covered by water. This is analogous to a tumor with overall high oxygenation levels. The waves, which represent fluctuations in red blood perfusion, have little-to-no effect on the oxygenation of the cells in various parts of the tumor since there is sufficient oxygen to begin with. During low tides, however, most of the island would be exposed. Fluctuations in red blood flow (waves) would have a larger effect on how oxygenated the cells are when there is low overall oxygenation, and this can lead

to cycling hypoxia. This is exhibited by how parts of the island are exposed at the wave troughs, but not at wave crests.

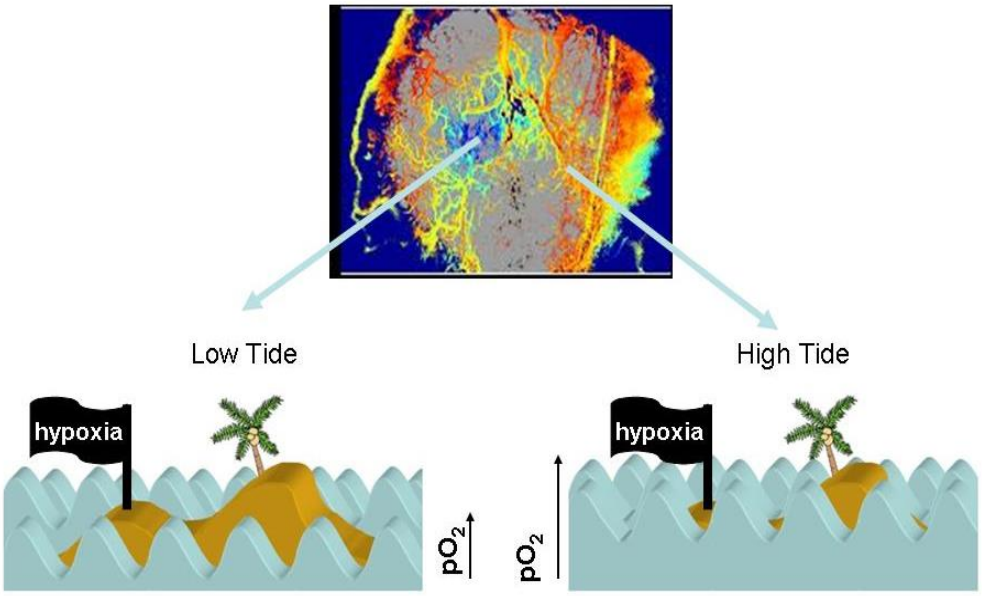

Figure 1.1: Using tides and waves as an analogy of cycling hypoxia. The upper panel is a map of the hemoglobin saturation in a tumor, with red indicating high saturation and blue indicating low saturation. The lower panel is an illustration of the analogy as applied to this tumor. Well-oxygenated regions (high tide) would be less susceptible to changes in blood perfusion (waves), but less well-oxygenated regions (low tide) can easily become hypoxic (more of the island is exposed at wave troughs). Reproduced with permission from Dr. Mark W. Dewhirst.

Chronic and cycling hypoxia can affect tumor growth in different aspects, but both have been shown to endow tumors with increased radio- and chemo-resistance.[9] Photon therapy, for example, is thought to be reliant on oxygen radicals near the tumor cells to induce unrepairable breaks in DNA strands.[11] Under optimal conditions, the break would either be repaired incorrectly or not at all, which would then induce cell death, inhibiting their proliferation. In

hypoxic environments where there is lower pO_2, the probability of producing an oxygen radical will thus decrease, reducing the probability of tumor cell death. Beginning with Gray *et al.*'s landmark study in 1953, multiple *in vitro* and *in vivo* studies have demonstrated the significance of oxygen concentration in determining radiation response.[12–14] Hypoxic tumors were shown to have higher cell survival both *in vitro* and *in vivo* when irradiated as compared to normoxic tumors. Reinhold *et al.* went a step further to demonstrate how chronic and acute hypoxia lead to persistent and transient radioresistance respectively; this proved that both affected radiotherapy treatment response.[11] Clinically, hypoxia in the tumor microenvironment is often correlated with poor patient prognosis.[15] It has been demonstrated to increase the rate of cancer metastasis, and enhance both radio- and chemo- resistance, in turn rendering most current therapeutic options less effective.

1.2 Clinical Problem – Hypoxia in Breast Cancer

Breast cancer is estimated to be the number one type of cancer incidence in 2018 amongst women in the United States, and the second leading cause of cancer-related deaths.[16] Early non-metastatic breast cancers are readily treatable and tend to have high survival rates; on the other hand, poor prognosis is significantly associated with metastatic breast cancers, which are less common.

Breast cancers that present with metastasis are usually incurable, and metastatic tumors are responsible for 90% of breast cancer-related deaths.[17,18]

The potential of breast cancer to turn metastatic is thought to be dependent on several factors, including, but not limited to, breast cancer subtype and hypoxia. Breast cancer is usually divided into 4 subtypes, depending on the types of receptors expressed on the cancer cells. These are: Luminal A, Luminal B, HER2+ve, and Basal/Triple Negative breast cancers. HER2 stands for human epidermal growth factor 2. Basal and triple negative breast cancers are not synonymous; however, they both lack, or present low levels of, hormone receptor expression as well as HER2 receptor expression. Table 1.1 shows a summary of the receptors present for each subtype.

Table 1.1: Presence of Receptors in Different Subtypes of Breast Cancers

Subtype	**Hormone Receptor**		**HER2 Receptor**	**Notes**
	Estrogen Receptor (ER)	Progesterone Receptor (PR)		
Luminal A	+	+	-	ER and/or PR present
Luminal B	+	+	+	ER and/or PR present
HER2+ve	-	-	+	
Basal/Triple Negative	-	-	-	

Multiple population studies have demonstrated that Luminal A breast cancers are the most prevalent, but also have the highest survival rate. On the

other hand, basal and triple negative breast cancers are fairly common and have the lowest survival rate of the four subtypes.[19,20] The subtype of breast cancer is also a factor for metastatic potential and locations of distal metastasis. For example, Luminal A, Luminal B and HER2+ve breast cancers are more commonly associated with lung metastasis, but this is not the case for basal and triple negative breast cancers. Basal and triple negative breast cancers have also been demonstrated to have one of the highest metastatic propensities, and consequently cause a disproportionately large number of breast cancer-related deaths.[19,20]

Another major factor in metastatic potential of cancers, breast cancer notwithstanding, is hypoxia. Hockel *et al.*'s clinical trial in 1996 was one of the earliest demonstrations that tumor oxygenation can be used as a prognostic marker of cancer progression – the results, from a pool of 103 patients, had shown that hypoxic uterine tumors (median $pO_2 < 10$ mm Hg) were significantly more aggressive than nonhypoxic ones (median $pO_2 \geq 10$ mm Hg), and that the 52 patients with hypoxic tumors had a significantly worse overall survival.[21] With the use of diffuse reflectance spectroscopy, Nakamiya *et al.* also demonstrated that hypoxia in breast cancers also had a similar correlation to poor patient outcome.[22] Henceforth, multiple studies have sought to understand how hypoxia influences metastasis, but with mixed success. However, the

consensus is that hypoxia activates certain transcriptional genes such as hypoxia-inducible factors, and high expressions of these are, in turn, correlated with undesirable prognosis.[4,21,23]

Hypoxia and breast cancer subtype are not independent factors of metastasis. Triple negative breast cancers have been shown in clinical trials to be more hypoxic than other breast cancer subtypes.[24] The expression of HIF-1α, which is normally stabilized by hypoxic conditions, has also been found to be more prevalent in basal and triple negative breast cancers.[24] The presence of HIF-1α is associated with more aggressive metastasis and higher cancer cell survival rates under hypoxic conditions. Notably, the expression of HIF-1α has been found to remain overexpressed in basal and triple negative breast cancers even under normoxic conditions.[24]

Many breast cancers are treated with a variety of methods comprising of chemotherapy, hormonal therapy, and radiation therapy. However, for basal triple negative breast cancers, the lack of hormone receptor expression means that hormonal therapy is ineffective. While chemotherapy is commonly employed, recurrence rate still tends to be fairly high, and these recurrences are often accompanied by metastasis.[25] The tendency for these cancers to both be more hypoxic when compared to other tumors, and also have higher baseline levels of HIF-1α, renders them more resistant to current treatment options. It is

therefore critical to understand the combined effects of radiation and hypoxia in this subtype of breast cancer.

Boron nanoparticles conjugated with folic acid may prove useful in this regard since triple negative cell lines have a significant overexpression of the folate receptor, FOLR1, as compared to other breast cancer cell lines.[26,27] O'Shannessy *et al.* reported in 2012 that compared to ER/PR positive and HER2 positive breast cancer cell lines, triple negative cell lines have a much higher expression of FOLR1.[26] This was later corroborated by Necela *et al.*, who investigated both mRNA and protein-level expressions of FOLR1 in breast cancer cells.[27] FOLR1 is also expressed on normal epithelial breast cells, but is not found in any other normal breast cells.[28] This indicates that FOLR1 can be a useful target for breast cancer diagnostic and therapeutic applications, especially in triple negative breast cancers.

1.3 Imaging Hypoxia

Given these far-reaching implications of hypoxia in cancer cells when it comes to both prognosis and treatment, managing hypoxia becomes critical for improved patient survival. The first step towards this goal is to develop techniques to quantitatively image hypoxia. However, attempts to image hypoxia have been met with many complications. A brief review of employed

methods is in order to understand where current oxygen-sensing technology stands in relation to these complications. Table 1.2 gives an overview of these methods.

Table 1.2: Overview of Current Oxygen-Sensing Technologies (adapted from Roussakis *et al.*)

Technique	Physical Principle	Advantages	Limitations
Polarographic Electrode	Generation of electric current when reduced in presence of oxygen	Direct quantification of pO_2	Removes O_2 from environment, invasive, not repeatable, only at particular spatial location
Radioisotope Imaging	Use of contrast agents that undergo redox reactions in presence of O_2	Full-body imaging, non-invasive	Indirect, low spatial and temporal resolutions, short-lived radiotracers
Resonance Imaging	Difference in signal dephasing between deoxygenated and oxygenated hemoglobin	Non-invasive	Indirect, low spatial and temporal resolution
Optical Imaging	(1) Differences in absorption spectra of deoxygenated and oxygenated hemoglobin (2) Luminescence quenching	High spatial and temporal resolution, non-invasive For (2), direct quantification of pO_2	Limited light penetration, poor spatial coverage For (1), indirect, dependent on blood perfusion

Recognized as the "gold standard" in oxygen-sensing operations, the polarographic electrode consists of cathodes that generate electric current when

reduced in the presence of oxygen.[29] The direct proportionality of current to the partial pressure of oxygen makes it convenient to calculate oxygen concentration levels from collected measurements. However, the main limitation of these electrodes is that they are invasive and hence unfeasible for real-time patient imaging. Further, the electrodes only record the oxygen concentration at a specific point – spatial distributions of oxygen concentration, which are critical to understanding the cyclical nature of hypoxia, cannot be obtained using this method.[29] The consumption of oxygen also makes repeat measurements impractical.

To overcome these limitations, newer techniques running the gamut from radioisotope and magnetic resonance imaging to optical imaging have been developed. Non-invasive radioisotope techniques like Positron Emission Tomography (PET) and Single Photon Emission Computed Tomography (SPECT) allow the entire body to be imaged while being non-invasive. They involve contrast agents like ^{18}F-fluoromisonidazole (^{18}F-MISO) and ^{18}F-fluoroazomycin-arabinoside (^{18}F-FAZA) that can be injected into the patient.[29] Such contrast agents undergo redox reactions in the presence of oxygen and are then transported away; conversely, in hypoxic regions where there is insufficient oxygen for oxidization to occur, these contrast agents bind to intracellular components. PET and SPECT imaging is then conducted several hours post-

injection to allow time for the contrast agents to accumulate in hypoxic regions.[29] The core limitations in these techniques are the low temporal and spatial resolutions. Studies that require good resolution in both dimensions in order to observe small pockets of hypoxic regions and/or cyclic hypoxia would not be able to use these techniques. These methods are also quite expensive.

Resonance imaging, which includes both nuclear magnetic resonance and electronic resonance imaging, utilizes magnetic fields to perturb the electromagnetic field of the nuclei involved. In nuclear magnetic resonance imaging, oxygenation in the microenvironment is indirectly measured by imaging deoxygenated hemoglobin. Deoxygenated hemoglobin is paramagnetic and will increase proton dephasing. This reduces signal, which serves as contrast against areas with oxygenated hemoglobin that do not affect proton dephasing. When imaging hypoxia, contrast agents that change the relaxation period of hypoxic regions are used. However, as with PET and SPECT, resonance imaging also suffers from relatively poor resolution since it cannot resolve small regions of hypoxic regions within a single tumor.

Electron paramagnetic resonance (EPR) oximetry measures electron spin dephasing rather than proton spin dephasing. Oxygen molecules are paramagnetic, and the addition of contrast agents serve to improve sensitivities and signal-to-noise ratios for oxygen sensing applications via EPR oximetry.[29]

Environments with higher oxygen concentration yield broader spectral peaks; EPR oximeters depend on this broadening to quantify oxygen concentrations.[30] Currently, EPR techniques have largely been used in the preclinical context, but efforts have been made to advance it into more clinical applications. Rickard *et al.* notes that there are currently several ongoing clinical trials that utilize EPR imaging or oximetry.[30]

Optical methods for imaging hypoxia are usually based on one of the following principles: differences in absorption spectra due to oxygen binding to hemoglobin, or luminescence quenching in the presence of oxygen.[29] Oxygenated hemoglobin and deoxygenated hemoglobin have different absorption spectra within the visible light spectrum, and the differences in spectra can be used to calculate oxygen saturation. Techniques that utilize this principle include pulse oximetry, diffuse optical spectroscopy and tomography, optical coherence tomography, and photoacoustic tomography. However, these techniques are dependent on blood perfusion, and are unable to give a direct measurement of the concentration of dissolved oxygen in the intercellular space. Rather, they provide information on the state of oxygen delivery in the tumor microvasculature. This can still be useful in hypoxia imaging studies: Palmer *et al.* have described how the use of hyperspectral imaging can be used in conjunction with oxygen-dependent luminescence quenching in nanoparticles to

quantify both oxygen delivery and tissue oxygen tension to further understand hypoxia dynamics.[3] Hu *et al.* have also utilized this technique to illustrate that trends in vascular oxygenation of head and neck cancer during and after fractionated radiotherapy can predict how well the tumor is controlled.[31]

Luminescence quenching refers to the phenomenon where oxygen in the environment competes with long-lived phosphorescence. Phosphorescence is the emission of photons when electrons in an excited triplet state relax to the ground state. This differs from fluorescence, which is short-lived and refers to the photon emitted when an excited electron in the singlet state relaxes to the ground state. In some molecules, phosphorescence is readily susceptible to quenching – when there is oxygen, the excited electron may collide into an oxygen molecule in the triplet state and transfer its energy to form singlet state oxygen molecules. This energy transfer quenches the luminescence process, as described by the Stern-Volmer equation[29]:

$$\frac{I_0}{I} = \frac{\tau_0}{\tau} = 1 + k_q \tau_0 pO_2 \qquad [1]$$

Here, I and τ refer to the intensity and the lifetime of the luminescence at a given partial oxygen pressure, pO_2, and quenching constant k_q. The 0 subscript indicates the absence of oxygen. A simplified Jablonski diagram is also shown in Figure 1.2 to illustrate luminescence and luminescence quenching.

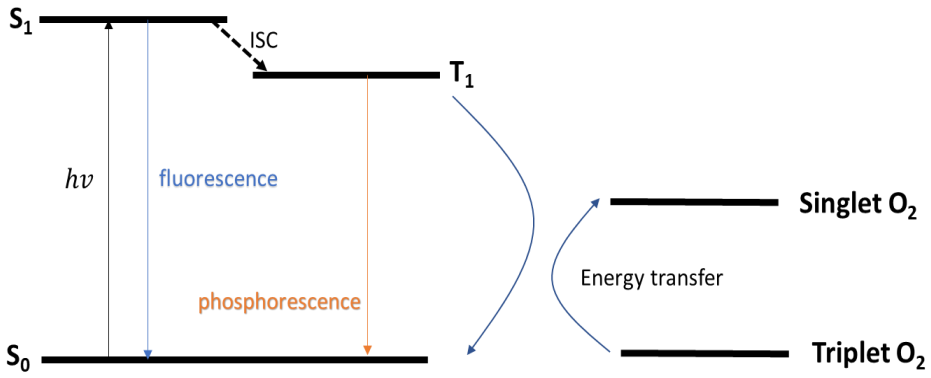

Figure 1.2: Simplified Jablonski Diagram. When an external photon interacts with the system, an electron is excited from the ground state to an excited singlet state. The excited electron can either return to the ground state by emitting fluorescence, or change its spin and transition to the triplet state through intersystem crossing (ISC). The release of a photon when an electron relaxes from a triplet state is known as phosphorescence. However, phosphorescence can also be quenched by other molecules like oxygen via various energy transfer processes; this is known as luminescence quenching.

As such, both the intensity and the lifetime of the luminescence change according to the amount of oxygen available in the environment. Methods that utilize luminescence quenching to quantify oxygen concentration would then have to detect either changes in intensity or lifetime. In the former, the fluorescence intensity of the probe would have to be calibrated to various oxygen concentrations separately. However, signal-to-noise ratios have to be sufficiently high for this method to be feasible.

In view of these limitations, Zhang *et al.* describe an innovative way to utilize luminescence quenching – designing a dual-emissive nanoparticle that would allow one to use ratiometric sensing.[32] In ratiometric sensing, the oxygen-

dependent luminescence is compared with another oxygen-independent photon emission. The ratios are then used to quantify the oxygen concentrations. This reduces the problem of high background noise in fluorescence detection. However, most ratiometry methods require at least two different fluorescent particles to be present, which complicates the calibration process since emissions from two different particles have to be tuned. A dual-emissive single-component nanoparticle resolves this problem.[32] The nanoparticle is excited by a single wavelength, and then emits two separate wavelengths, of which one is oxygen-dependent, and the ratio of their respective intensities can be used to quantify oxygen concentration. Our oxygen-sensing boron nanoparticle is one such example.

1.4 Boron Nanoparticles

Our collaborators at the Fraser lab at the University of Virginia have developed various types of boron nanoparticles, with which we have conducted experiments to determine their utility in quantitatively imaging hypoxia. The dual-emissive boron nanoparticle has a fluorescence and oxygen-dependent phosphorescent peak, and we have previously established its ability to quantify oxygen concentration *in vivo* semi-continuously over the course of an hour.[3] More recently, the lab has developed boron nanoparticles conjugated with folic

acid. The second part of this thesis is primarily concerned with testing these particles' effectiveness in targeting the folate receptor FOLR1, which are more frequently expressed in breast and ovarian cancer cells than in normal cells. The BNPs used for the second project are not oxygen-sensing, but the eventual goal is to conjugate oxygen-sensing BNPs with folic acid.

1.4.1 Dual-Emissive Boron Nanoparticles

Zhang *et al.* had previously reported on a boron nanoparticle (BNP) that has stable fluorescence at approximately 460nm and oxygen-dependent long-lived phosphorescence at approximately 560nm. Ratiometric sensing can thus be employed to quantify the oxygen consumption rate of cells. These nanoparticles are also tunable in that the intensities of the fluorescence and phosphorescence can be changed by altering the molecular weight.

The nanoparticles can be used to quantify oxygen concentration by means of obtaining the fluorescence to phosphorescence ratio. Since fluorescence is stable across oxygen concentrations while phosphorescence is quenched in high oxygen conditions, the fluorescence to phosphorescence ratio can be utilized to minimize noise in the signal, as opposed to using only the oxygen-dependent phosphorescence to measure oxygen concentration. This ratio can also be calibrated at a range of oxygen concentrations prior to an experiment.

Figure 1.3 shows spectroscopy data obtained from one type of the developed BNPs, normalized to the fluorescence peak at 460nm. When the concentration of oxygen that is bubbled into the BNPs increases, the phosphorescence peak decreases significantly.

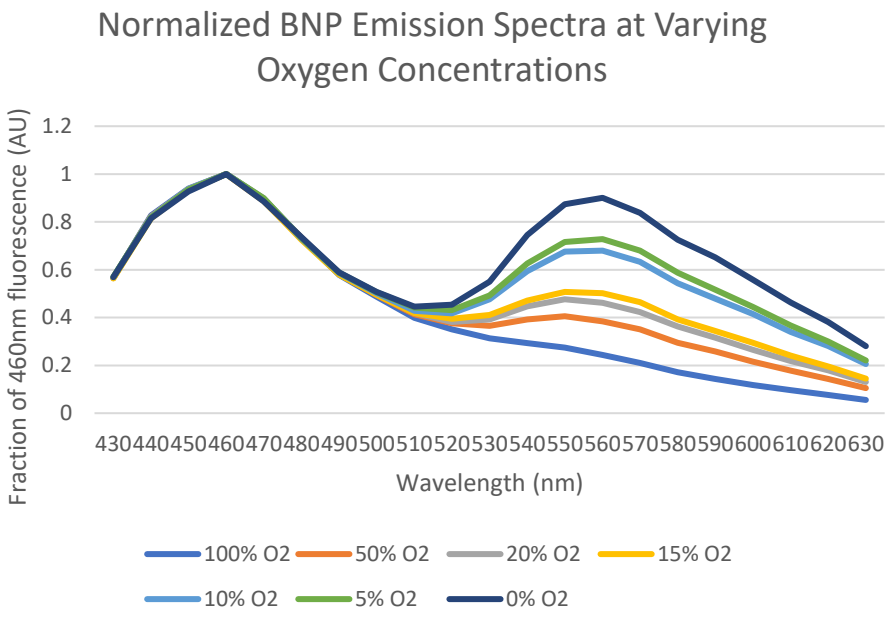

Figure 1.3: Normalized Emission Spectra of Oxygen-sensing BNPs. Under higher oxygen concentrations, phosphorescence signal is decreased due to quenching.

1.4.2 Boron Nanoparticles Conjugated with Folic Acid

Another equally critical problem in developing nanoparticles to image hypoxia is determining how best to target cancer cells – this would improve signal-to-noise ratios, and also open up the possibility of intracellular sensing. One way to achieve this is to functionalize the nanoparticles. Past studies have demonstrated that cancer cells often overexpress certain

receptors on their cell surface that are absent or minimally present on normal cells. The folate receptor FOLR1, which is extremely common in both ovarian cancer cells and breast cancer cells, tends to be overexpressed in triple negative breast cancer cells.[27]

Folic acid has a strong affinity to FOLR1, and the resulting complex has a much lower dissociation constant than the complex formed between FOLR1 and naturally-occurring folate.[33] The folic acid compound is then internalized into the cell via the endocytotic pathway.[34] This makes folic acid an ideal conjugate for targeting FOLR1, and many studies have demonstrated its feasibility in targeting other high FOLR1-expressing cancer cells.[35–38] Our collaborators have synthesized boron nanoparticles with folic acid ligands (BNP+FA) that would theoretically enhance uptake in cells overexpressing FOLR1. The second part of this thesis project aims to determine its efficacy in targeting FOLR1-expressing cancer cells.

1.5 Spectral Imaging

Using oxygen-sensing BNPs to quantify oxygen consumption rests on the assumption that emission photons can be collected and separated into appropriate channels of wavelengths. Currently, there are several technologies that can be used to perform this.

One common method for separating spectra during imaging is through the use of tunable filters. Tunable filters can be electronically controlled such that only specific wavelengths of the spectra are transmitted to the sensing devices. Currently, there are two main competing types of tunable filters, each with its own advantages and limitations. Abdlaty *et al.* have compared the performance of these two filters in terms of various performance characteristics like image quality, speed, and spatial resolution.[39] These findings are summarized in Table 1.3.

Table 1.3: Overview of Common Tunable Filters

Type	Working Principle	Advantages	Limitations
Liquid-Crystal	Electronic birefringence	Superior image quality, simpler operations	Poorer spectral resolution, slower access to spectral bands, less efficient out-of-band suppression
Acousto-Optical	Diffraction	Higher spectral resolution, more rapid tuning, more efficient out-of-band suppression	Poorer image quality, more complicated operations

Liquid-crystal tunable filters rely on electronically-tunable birefringent materials to separate spectra. Materials are birefringent when their refractive index is dependent on the polarization and direction of the incident light. Liquid-crystal tunable filters utilize birefringent filters comprised of stacks of polarizers

and liquid crystal plates.[40] Liquid crystal variable retarders, which are electronically controlled, are utilized to tune the refractive properties of the liquid crystal, thereby selecting particular wavelengths for transmission.[41]

As implied by its name, the acousto-optical tunable filter is based on photoacoustic interactions.[39] A piezoelectric transducer is usually attached to a crystal; a radiofrequency signal drives this transducer to produce acoustic waves that are transmitted through the crystal.[39] The crystal's refractive index is modified as the acoustic wave passes through since it develops compression and tension zones.[39] Incoming radiation would then be subjected to diffraction and polarization, effectively giving rise to the transmission of a narrow band of wavelengths.[28]

Another available technology in spectral imaging is the Quadview multichannel system, developed by Photometrics. Rather than obtaining spectra wavelength by wavelength, the Quadview system acquires the entire emission spectra, splits it into four different channels through a series of beam splitters, and projects each channel onto a quadrant of the charge-coupled device simultaneously.[42] This allows simultaneous imaging of both fluorescence and phosphorescence, which is an advantage over tunable filters.

The Palmer Lab has both the Quadview multichannel system as well as a liquid-crystal tunable filter. Spectral component separation using a parallel factor

analysis (PARAFAC) algorithm revealed that compared to the Quadview, the liquid-crystal tunable filter offers better spectral separation – there is a much larger range of channels for which either fluorescence or phosphorescence dominates. This is illustrated in Figure 1.4, which shows the spectral decomposition of oxygen-sensing BNPs by channel for each method.

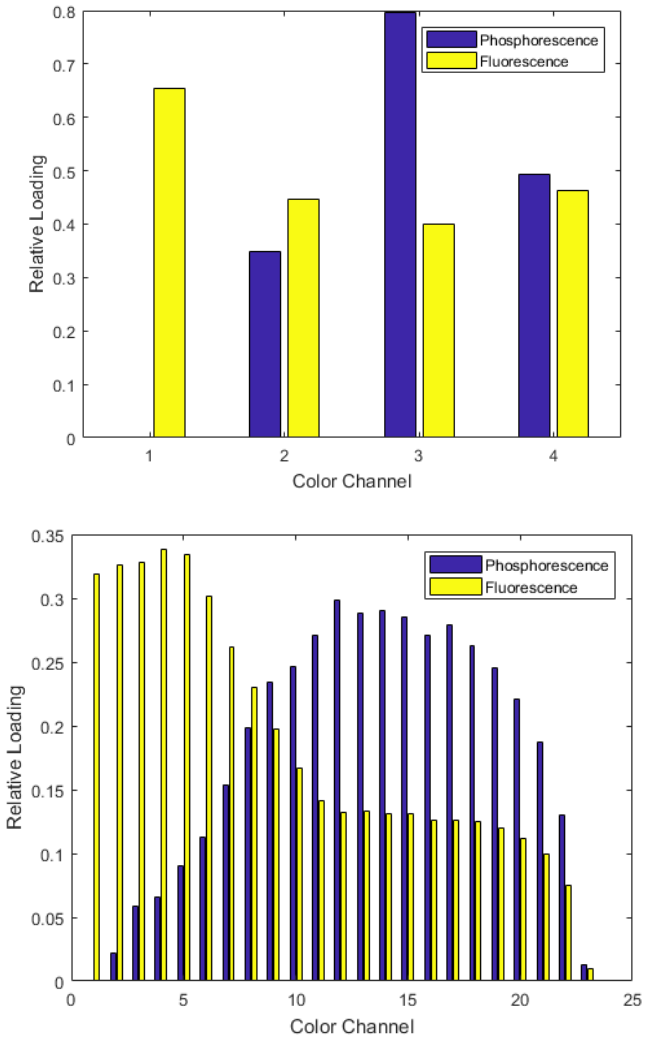

Figure 1.4: Relative fluorescence and phosphorescence loading in each color channel for each technique when imaging BNPs. Some fluorescence signal is present in channels dominated by phosphorescence for both techniques, but is more prominent in the Quadview. (Top) Separation via Quadview; (Bottom) Separation via Liquid-Crystal Tunable Filter

Nevertheless, the Quadview system is still suitable for imaging dual-emissive BNPs, since phosphorescence signal is still clearly dominant in the third channel of the Quadview system. Therefore, BNP projects in this work were imaged using the Quadview.

2 Quantification of pO_2 and hemoglobin saturation in irradiated mice tumors using boron nanoparticles and optical imaging

2.1 Introduction

Tumor hypoxia has long been demonstrated to promote cancer metastasis, chemoresistance, and radioresistance, thereby adversely affecting patient prognosis. Reoxygenation, a phenomenon where the tumor microenvironment become less hypoxic post-radiation, can be leveraged to mitigate this problem.[43] It has been theorized that immediately after radiation, the majority of the remaining tumor are radio-resistant hypoxic cells because the well-oxygenated tumor regions have responded to the radiation. These hypoxic tumors will, over time, become reoxygenated; multiple *ex vivo* studies have demonstrated that the hypoxic fraction of various tumors spikes to nearly 100% post-irradiation, then decreases thereafter.[12,43–45] Fractionated radiotherapy exploits this phenomenon of reoxygenation by splitting the total radiation dose, allowing time for the tumor cells to become less hypoxic and, consequently, less radioresistant. This theoretically improves the effectiveness of radiation therapy.

Oxygen-sensing polarographic electrodes have been employed in a multitude of studies to measure oxygenation in a variety of tumors, even until fairly recently.[13,23,46–48]

These studies have firmly established the correlation between tumor hypoxia and poor patient prognosis – Brizel *et al.,* Rudat *et al.* and Nordsmark *et al.* have all conclusively demonstrated the prognostic power of tumor oxygenation in head and neck cancer patients.[13,23,48] Hockel *et al.* also showed that there was a strong correlation between hypoxia and malignant progression of uterine cancer.[46] The ability to understand tumor oxygenation processes is thus of significant clinical interest.

Vujaskovic *et al.* have more recently utilized these polarographic electrodes to demonstrate reoxygenation in breast cancers after irradiation and hyperthermia; however, there are severe limitations in the use of the electrodes.[47] While the polarographic electrode offers a precise measurement of oxygen concentration, its consumption of oxygen in the process of measurement limits its use in serial studies.[29] Consequently, while the phenomenon of reoxygenation can, and has, been demonstrated in a variety of studies including Vujaskovic's, its kinetics would have to be quantitatively elucidated through other means.[12,44,45,47] An ideal technique for serial quantitative assessment of tumor oxygenation would include, amongst others, the following characteristics: 1) able to directly and accurately quantify tumor oxygen tension; 2) possesses high resolutions in both temporal and spatial domains; 3) is non-invasive; 4) does not perturb the tumor microenvironment, and; 5) induces few artifacts. There has

been a host of techniques, running the gamut from full-body radioisotope and resonance imaging techniques to optical imaging systems, developed for oxygen-sensing applications both preclinically and clinically.[29,49] Diffuse reflectance spectroscopy has recently garnered interest for its ability to non-invasively quantify hemoglobin saturation, which can serve as a marker for vascular oxygenation.[50–52] This technique has been employed by Ueda *et al.* to investigate eribulin-induced reoxygenation in breast cancer, and also by Diaz *et al.* who similarly investigated radiation-induced reoxygenation in head and neck squamous cell carcinoma.[51,52] However, one key limitation remains – hemoglobin saturation is not a direct indicator of oxygen tension in tumors. There remains a curious lack of a single technique that can directly quantify oxygenation in tumors serially, and with adequate spatial and temporal resolutions.

Recently, Palmer *et al.* have pioneered a method that combines hyperspectral imaging of hemoglobin absorption with dual-emissive boron nanoparticle (BNP) fluorescence imaging to quantify both vascular oxygenation supply and tissue oxygen tension.[3] Dual-emissive BNPs, which exhibit short-lived fluorescence and long-lived phosphorescence, measures the extent of phosphorescence quenching for oxygen concentration quantification.[32] Oxygen sensors that leverage oxygen-dependent phosphorescence for pO_2 quantification often rely on phosphorescence lifetime (τ). Examples of oxygen sensors under development that utilize phosphorescence lifetime include an iridium probe, presented by Hirakawa *et al.* as well as a platinum-

porphine/poly(perfluoroether) film described by Zhao *et al*..[53,54] However, ratiometry methods involving multi-emissive nanoparticles offer advantages over these systems – ratiometry methods do not require specialized detection instrumentation commonly needed for phosphorescence lifetime imaging. In addition, dual-emissive boron nanoparticles offer several advantages over single-emissive oxygen-sensing nanoparticles. By calculating the ratios of stable fluorescence to phosphorescence as a marker of oxygen concentration, the effects of nanoparticle degradation and emission fluctuations, as well as the dependence on nanoparticle concentration, can be disregarded.[3] When injected into tumors or topically applied, these BNPs allow direct quantification of oxygen concentration within the tumor microenvironment with high spatial and temporal resolutions. BNP imaging also does not present perfusion artifacts that are more significant in hemoglobin saturation imaging methods. However, this is not to say that hemoglobin saturation imaging methods are irrelevant; when dual-emissive BNP fluorescence imaging is combined with hemoglobin saturation imaging, simultaneous quantitative investigation into the oxygen supply and demand within the tumor microenvironment becomes possible. This potentially opens up new avenues of research into hypoxia and reoxygenation dynamics.

The purpose of this work is twofold. By employing the two-pronged imaging method previously described by Palmer *et al.* to investigate the effect of

radiation on tumor hypoxia, it simultaneously validates the technology's capabilities in characterizing the microenvironments of tumors subjected to current cancer treatments (in this case, radiation therapy), while also providing further scientific insight into the kinetics of radiation-induced reoxygenation. To these ends, female C57BL/6 mice implanted with E0771 medullary breast tumors in dorsal window chambers were irradiated with a 12Gy dose in a single fraction. First isolated as a spontaneous tumor from C57BL/6 mice by Sugiura and Stock, the E0771 cell line is highly metastatic, immunosuppressive, and commonly grows attached to the peritoneal wall or the dermis.[55,56] Genomically, it has been classified as claudin low, which means that it is highly undifferentiated.[57] These characteristics allow it to mimic human breast tumors to a high degree while also allowing easy tumor assessments.[56] The oxygenation states of the tumors before irradiation and 48 hours after irradiation were measured using optical imaging. Parameters measured were then compared between the two different timepoints, and 2-way repeated measurements ANOVA statistical testing was performed to determine if there was significance for any of the changes.

2.2 Materials and Methods

2.2.1 Cell Culture

E0771 cells were cultured in L-Glutamine-containing Roswell Park Memorial Institute (RPMI) Medium (1X) with 10% FBS antibiotic-antimycotic. Cells were incubated at 37°C in a 5% CO_2, 95% air, humidified environment.

2.2.2 Tumor Implantation

All animal experiments were approved by the Duke University School of Medicine Institutional Animal Care and Use Committee. Dorsal chamber windows were surgically implanted onto dorsal skin folds of 40 female C57/BL6 mice (Charles River) according to the protocol reported by Palmer *et al*.[58] 100 000 E0771 cells in 20μl of RPMI were injected into the fascia of the tumor tissue within the dorsal window chamber of each mouse through a 30-gauge syringe. Mice were randomized into two groups – 20 mice were assigned to be irradiated with a single 12Gy dose, while the remaining 20 were assigned to be sham-irradiated. Mice were weighed thrice a week to check for abnormal weight loss. Due to complications such as premature death and abnormal tumor growth, only 12 mice from the irradiated group and 9 mice from the non-irradiated groups could be imaged at both timepoints.

2.2.3 Boron Nanoparticles

Iodine-substituted dye-polymer conjugate BF_2dbm(I)PLA and boron nanoparticle (BNP) aqueous suspensions were fabricated by the Fraser Lab at the University of Virginia according to previously reported methods.[59] Prior to injection into mice tumors, the BNPs were diluted in phosphate-buffered saline to obtain a nanoparticle concentration of $2.5 mg/ml$. $50 \mu l$ of this solution was then injected into the tumors through the tail vein at two timepoints: one day prior to irradiation, and two days post-irradiation.

2.2.4 Mice Irradiation

Mice were irradiated in an X-RAD 320 (Precision X-Ray) animal irradiator. Each mouse was subjected to 6.6 minutes of irradiation at 320kV, 10mA. The total dose delivered was 12Gy. Sham-irradiated mice were anaesthetized with 2.5% isoflurane, kept warm, and placed in the irradiator for the same duration of time without being subjected to radiation.

2.2.5 BNP Imaging

Mice were anaesthetized with 2.5% isoflurane via nose cone. BNPs were injected through the skin behind the window chamber into the chamber, such that they bathed the tumor surface, and fluorescence imaging (Zeiss Axio Observer Z1) was performed on the mice 1 hour after these injections. The mice were given 100% oxygen to inhale

through a nose cone for 3 minutes prior to each image acquisition, and kept on a heating pad throughout the imaging process. A long-pass filter was used to filter the excitation and emission spectra; excitation was centered at 430nm, while longer wavelengths from fluorescence and phosphorescence were allowed to pass through to the detector. To distinguish between the fluorescence and phosphorescence signal, the Q2 Quadview multichannel system (Photometrics) was used to split the emitted signal into 4 separate channels at 470nm, 505nm, 535nm, and 565nm, with a passband of approximately 30nm. These channels were projected onto a Hamamatsu Orca Flash4 CMOS camera.

2.2.6 Measurement of Hemoglobin Saturation

The general method used has previously been described by Palmer *et al*.[3] Hemoglobin (Hb) saturation of tumor vasculature was imaged on a Zeiss Axio Observer.Z1 microscope using an unfiltered white-light halogen light source in transmission mode. Emission wavelengths were filtered using a liquid-crystal tunable filter (VariSpec, Cri Inc., Woburn, MA) and recorded from 520nm to 620nm, at 10nm intervals.

2.2.7 Image Analysis

In the analysis of the fluorescent images, the method described in DeRosa *et al.* was used with slight modifications.[60] Raw images were first cropped to produce individual images of the fluorescence (F) and phosphorescence (P) signals. Background

correction was performed on these images with a calibration image and regions with low signal were removed with a mask. The images were then spatially aligned with a translational transformation. Ratios of the fluorescence image relative to the phosphorescence image (F/P) were calculated. The F/P images were then superimposed onto the brightfield images for visualization.

Hemoglobin saturation images were processed via a MATLAB program using the method described in Sorg *et al.*[50] The model proposed by Shonat *et al.* was used to correlate absorbance with concentrations of hemoglobin and deoxyhemoglobin.[61] This is described by Equation 2.1 below:

$$A_\lambda = \log\left(\frac{I_0}{I}\right) = \varepsilon_\lambda^{HbO_2} \cdot [HbO_2] \cdot L + \varepsilon_\lambda^{Hb-R} \cdot [Hb - R] \cdot L + SL \qquad [2.1]$$

In the equation, A_λ refers to the absorbance at wavelength λ, $[HbO_2]$ and $[Hb\text{-}R]$ refers to the concentration of oxy- and deoxyhemoglobin respectively, I refers to pixel value while I_0 refers to the pixel value of reference light, ε refers to the extinction coefficients corresponding to the subscript and superscript descriptions, L refers to path length, and SL refers to a path length-dependent scattering term. Absorbance values were converted from pixel values selected from regions without vasculature – these were assigned to be I_0. Since wavelengths were in the 520nm to 620nm range, the dominant absorbers in blood can be assumed to be oxy- and deoxyhemoglobin.

A least squares regression was used to solve the equation; calculated values of Hb saturation were either accepted or rejected depending on R^2 the coefficient of determination, which is described in Equation 2.2:

$$R^2 = 1 - \frac{SS_e}{S_t} \quad [2.2]$$

Here, SS_e is the sum of squared error, and S_t is the total variance.

2.2.8 Statistical Analysis

All statistical analyses were performed on GraphPad PRISM (version 8.0.1). Repeated measures 2-way ANOVA with Tukey's multiple comparisons tests were performed to determine significances in differences for F/P ratios and Hb saturation between tumors pre- and post-treatment. Pearson's r testing was performed to determine correlation between changes in F/P ratios and Hb saturation values pre- and post- treatment. An alpha-level of less than 0.05 was considered significant.

2.3 Results

Most irradiated mice tumors showed an increase in mean Hb saturation 48 hours post-irradiation; sham-irradiated mice tumors did not (Figure 2.1).

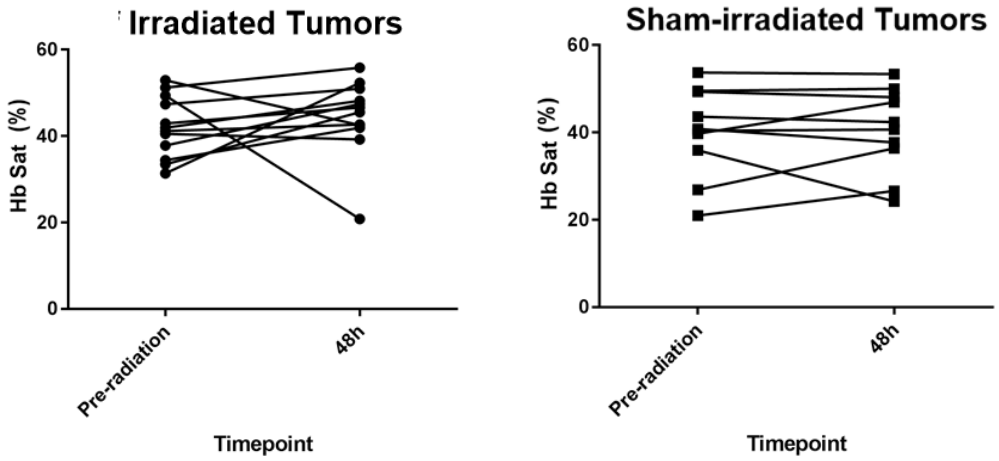

Figure 2.1: Changes in mean Hb saturation of individual mice tumors. (Left) Irradiated tumors; (Right) Sham-irradiated tumors

Figure 2.2 provides an example of a tumor demonstrating dramatically increased Hb saturation after irradiation. The top 2 panels are brightfield images of the tumor before and after irradiation, and the bottom 2 panels are Hb saturation maps. Brightfield images are at a higher magnification than Hb saturation maps, and the corresponding areas are highlighted in red boxes superimposed on the Hb saturation maps. Hb saturation is displayed on a color scale from blue (deoxygenated) to yellow (oxygenated). Pre-irradiation, central areas of the tumor appear to have lower Hb saturation, which suggests inefficient oxygen delivery. 48 hours post-irradiation, Hb saturation in the central portion of the tumor increases.

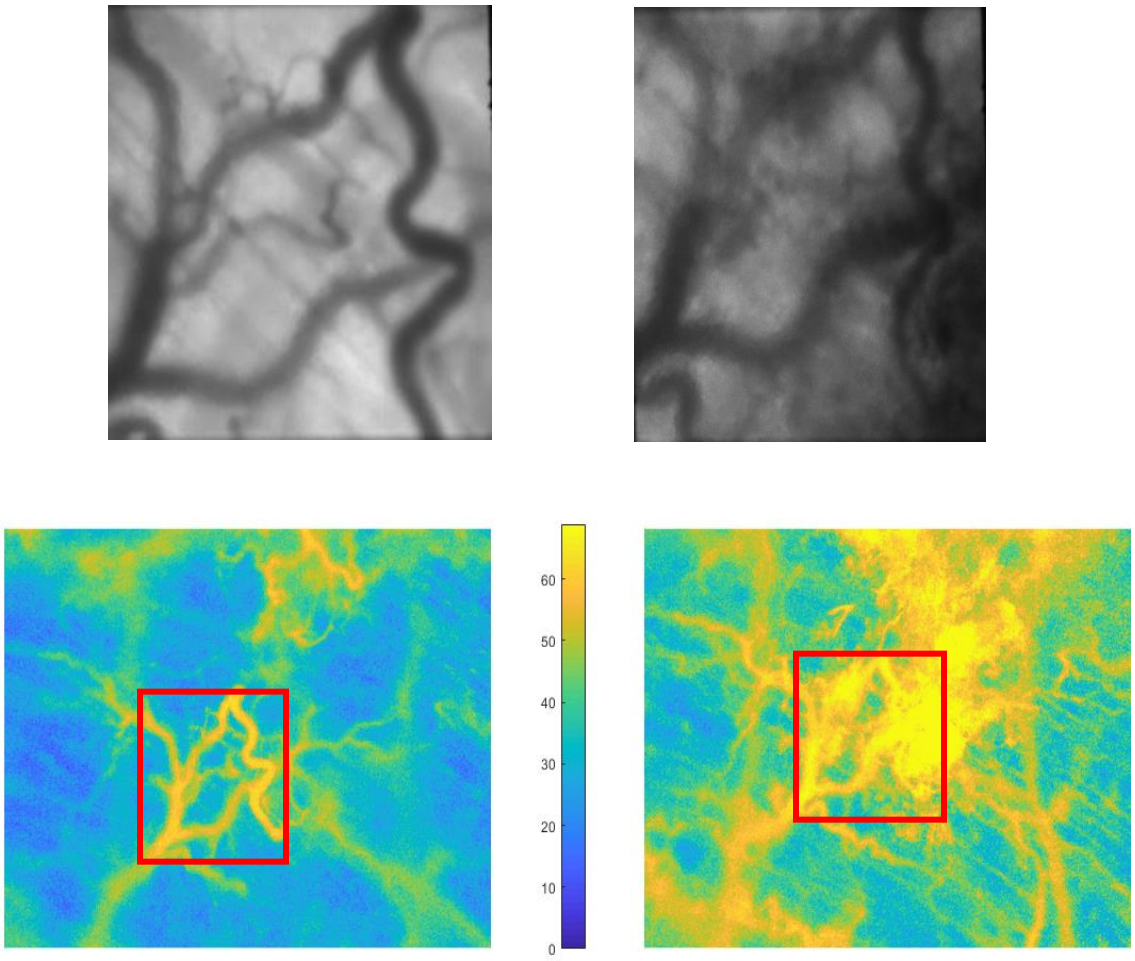

Figure 2.2: Example of an irradiated mouse tumor demonstrating increased Hb saturation. Hb saturation 48 hours post-irradiation increases, indicating an increase in oxygen delivery. The brightfield images demonstrate an increase in vasculature density on the topmost and rightmost areas of the frame post-irradiation, which also corresponds to an increase in hemoglobin saturation. (Top Left) Brightfield image pre-irradiation; (Top Right) Brightfield image post-irradiation; (Bottom Left) Hb saturation map pre-irradiation; (Bottom Right) Hb saturation map post-irradiation

In general, however, 2-way ANOVA testing showed that the observed increase in Hb saturation was not significant (Figure 2.3).

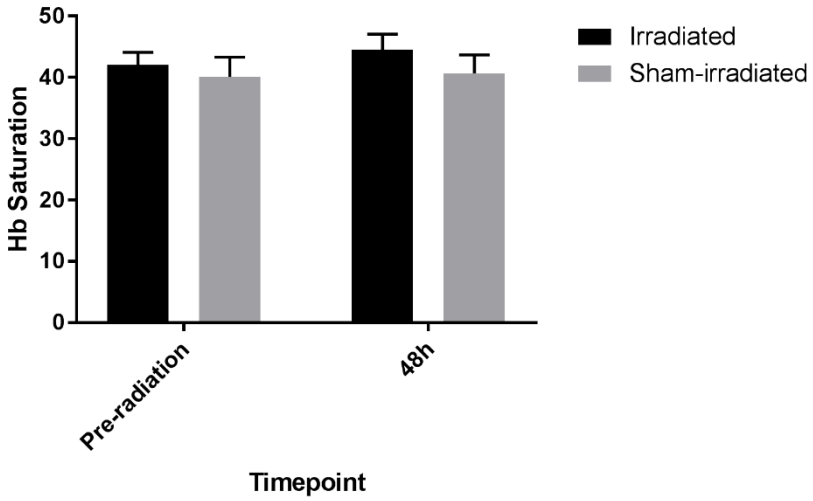

Figure 2.3: Average Hb saturation values of tumors at different timepoints. No significance was found between tumors before and after irradiation. No significant difference was found for sham-irradiated tumors pre- and post- treatment

Modest increases in mean F/P ratios were observed in irradiated mice tumors, with a caveat: mice tumors that originally had relatively high mean F/P ratios pre-irradiation tended to demonstrate a decrease in mean F/P ratios post-irradiation (Figure 2.4, left). Most sham-irradiated mice tumors had more inconsistent changes in mean F/P ratios pre- and post-irradiation (Figure 2.4, right).

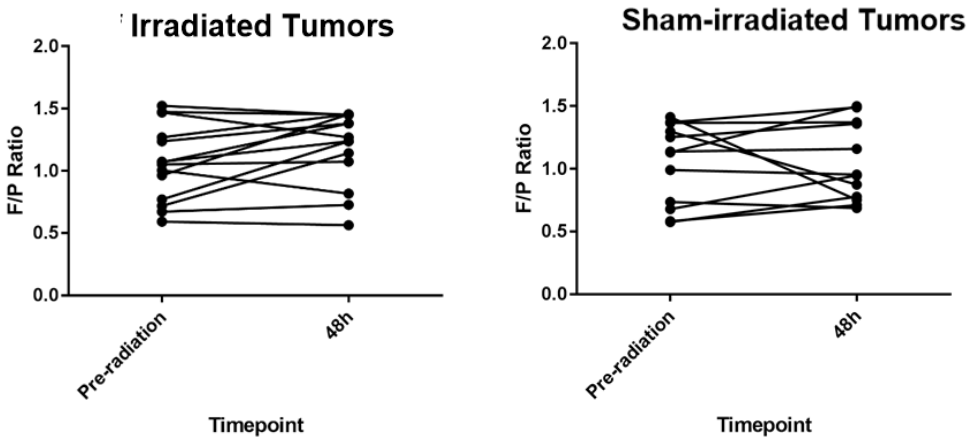

Figure 2.4: Changes in mean F/P ratios of individual mice tumors. (Left) Irradiated tumors; (Right) Sham-irradiated tumors

Figure 2.5 shows a tumor demonstrating an increase in F/P ratio post-irradiation.

Top panels contain brightfield images, while bottom panels contain F/P ratio maps.

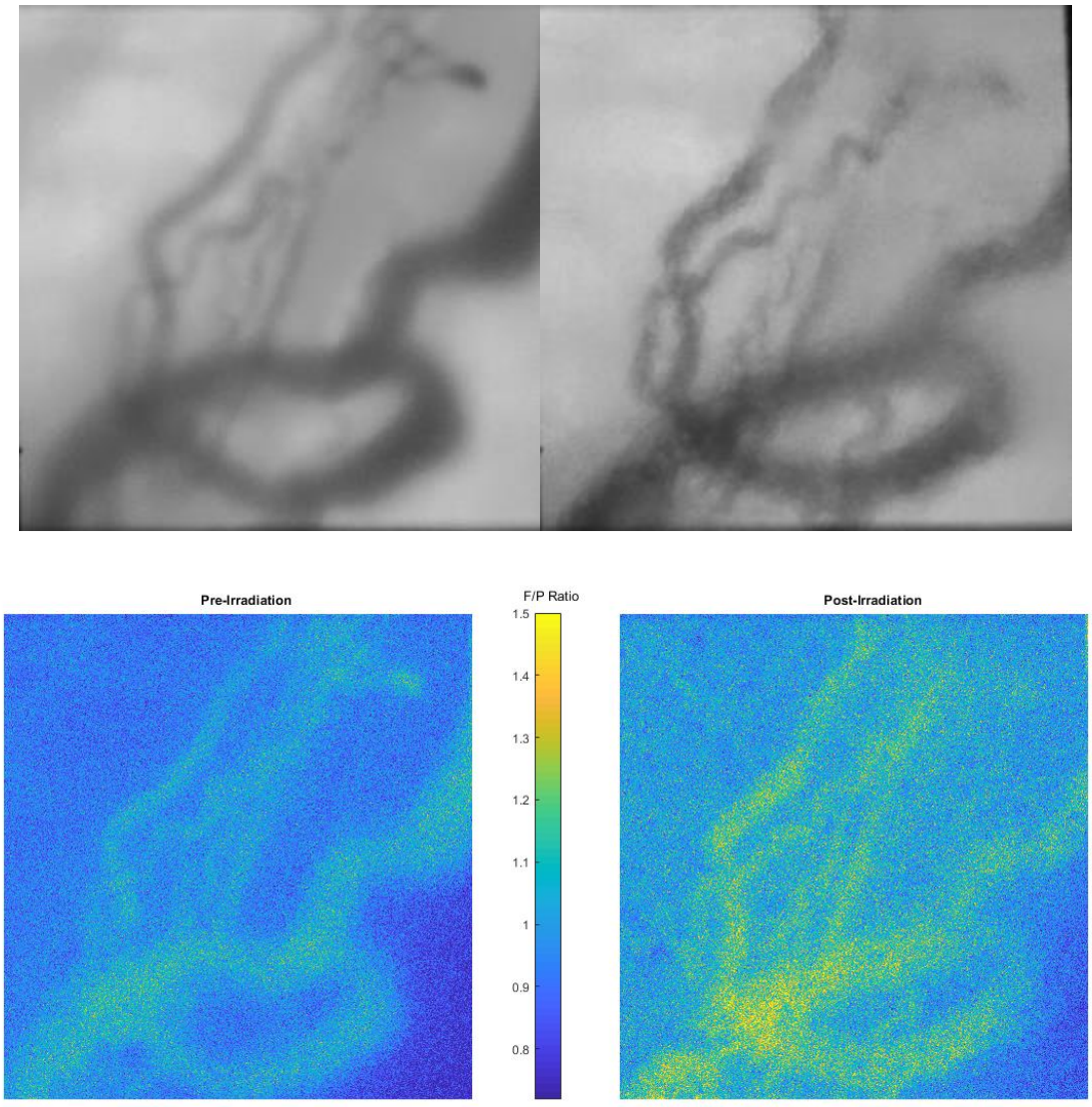

Figure 2.5: Example of an irradiated mouse tumor demonstrating increased F/P post-irradiation. The magnitude of the ratio increases post-irradiation, indicating an increase in tissue oxygen tension. Brightfield images show insignificant changes in vasculature density post-irradiation. (Top Left) Brightfield image pre-irradiation; (Top Right) Brightfield image post-irradiation; (Bottom Left) F/P ratio map pre-irradiation; (Bottom Right) F/P ratio map post-irradiation

Similar to the case of Hb saturation in Figure 2.2, F/P ratio is displayed on a color scale from blue (low F/P ratio) to yellow (high F/P ratio). Since phosphorescence is

quenched in the presence of oxygen, an increase in F/P ratio is indicative of increased pO_2.

Notably, unlike the data for Hb saturation, 2-way ANOVA testing revealed that increases in F/P ratios for irradiated tumors were significant ($p < 0.05$) (Figure 2.6). There were no significant changes in F/P ratio for sham-irradiated tumors.

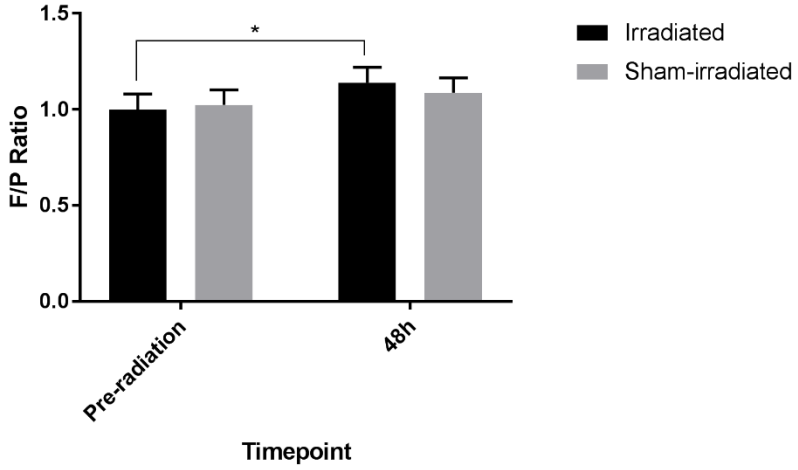

Figure 2.6: Average F/P Ratios of Tumors at Different Timepoints. 2-way ANOVA revealed significant differences ($p<0.05$) between the F/P ratios of irradiated tumors pre- and 48h post-irradiation. No significance was found for sham-irradiated tumors.

Figures 2.7 and 2.8 show the correlations between recorded mean F/P ratios and mean Hb saturation.

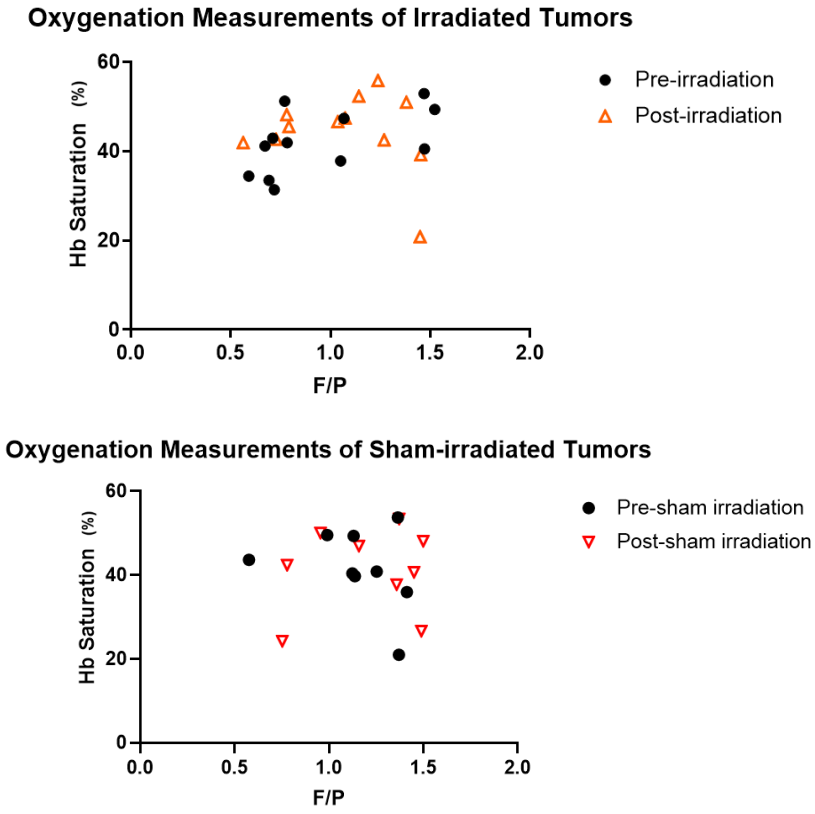

Figure 2.7: Graphs demonstrating how Hb saturation and F/P ratios in tumors change pre- and post- irradiation. In irradiated tumors, Hb saturation and F/P ratios post-irradiation both tended to be higher than baseline values; in sham-irradiated tumors, both measurements do not appear to change consistently between animals. (Top) Measurements for irradiated tumors; (Bottom) Measurements for sham-irradiated tumors

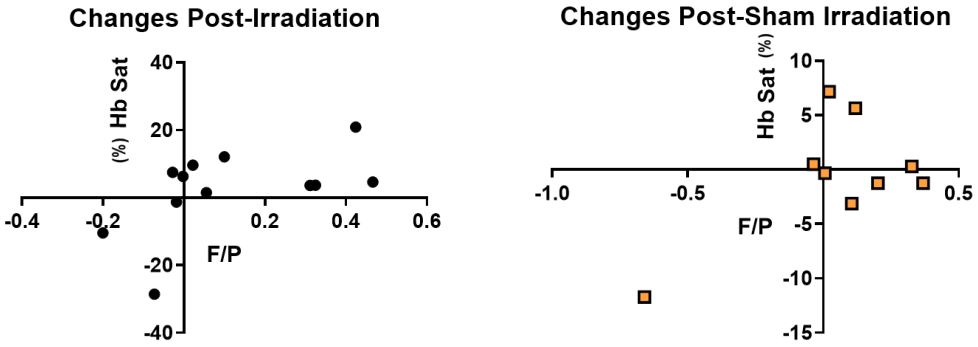

Figure 2.8: Graphs demonstrating absolute changes in measurements for each tumor. While Hb saturation increased in general for irradiated tumors, the extent of these changes was inconsistent with changes in F/P ratios. This lack of consistency was even more pronounced in sham-irradiated tumors, where increased F/P ratios were sometimes observed in tumors with decreased Hb saturation. (Left) Changes for tumors that were irradiated; (Right) Changes for tumors that were sham-irradiated

Responses of oxygen tension and Hb saturation to irradiation appear weakly related (Figure 2.7, top). Irradiated tumors that demonstrated increases in Hb saturation also tended to show increases in oxygen tension, and the inverse was also true (Figures 2.7, top panel, and 2.8, left panel). However, the extent of the increases between the two metrics do not appear to be correlated (Figure 2.8, left). A Pearson r test revealed weak correlations between the changes in F/P ratio and changes in Hb saturation values ($r = 0.5324$). Sham-irradiated tumors, on the other hand, demonstrated inconsistent trends in changes to Hb saturation and F/P ratios (Figures 2.7, bottom panel, and 2.8, right panel).

2.4 Discussion

There has been a dearth of techniques with adequate spatial and temporal resolutions that can be utilized for direct and serial quantification of tissue oxygen tension. This has hindered progress in quantitatively elucidating the mechanisms of tissue oxygenation and hypoxia. In this work, we have validated a new technique that rises to the challenge by directly quantifying tissue oxygen tension with high spatial and temporal resolutions. The presented data also offers a quantitative approach to investigate tumor reoxygenation post-irradiation, and adds to the body of literature by elucidating the mechanics of reoxygenation. Specifically, the results demonstrate that there is a significant increase in tumor oxygen tension 48 hours post-irradiation in E0771 tumors, evidenced by the significant increase in F/P ratios.

Conversely, vascular oxygenation – as indicated by hemoglobin saturation data – did not present a significant increase post-irradiation despite showing some signs of an increasing trend. This is most likely due to the presence of two mice tumors which demonstrated significant decreases in hemoglobin saturation. The decrease in hemoglobin saturation for these two mice were also mirrored in the corresponding F/P data, although to a much smaller extent. Curiously, there were also two other mice for which F/P decreased but Hb saturation increased.

The incongruencies between the changes in mean vascular oxygenation and mean tissue oxygen tension of the tumors post-irradiation suggests that the effects of

radiation on oxygen supply and demand may differ. While most of the mice demonstrated changes in the same direction for both F/P and Hb saturation data, the extent to which they change do not appear to be linearly related, as evidenced by the low correlation value. The presence of mice that demonstrated contradictory changes in oxygenation parameters also supports the notion that vascular oxygenation is not necessarily representative of tumor oxygen tension. Reoxygenation processes on this time scale post-irradiation appears to be a result of a decreased demand for oxygen, and may not be completely due to changes in vascular oxygen supply in the tumor. This finding serves only to underscore the importance of using a technique that can directly quantify tumor oxygen tension; indirect methods may only be measuring one of several contributing factors to tumor oxygenation and could miss out on the larger picture. A similar conclusion was also reached by Fenton *et al.*, who used immunohistochemical staining and perfusion marker methods to probe tumor and vascular oxygenation in KHT fibrosarcoma tumors 24 hours after a single 10Gy irradiation.[62]

Our observations lend credence to theories that attribute long-term reoxygenation to the overall reduction of tumor volume, allowing previously hypoxic areas of the tumor to fall within the oxygen diffusion distance of the nearest vasculature.[43] What we have observed in most of the E0771 tumors is likely a fall in demand for oxygen supply due to aerobic tumor cell kill, as well as easier access to oxygen supply for previously hypoxic areas of the tumor. This is also supported by

brightfield images, as in Figure 2.5 – there does not appear to be any significant structural changes to this tumor's vascular network post-irradiation.

The few tumor samples which had undergone dramatic increases in Hb saturation, one of which is shown in Figure 2.2, demonstrated significant structural changes in tumor vasculature. The tumor in Figure 2.2 shows a much denser vascular network in the central portion of the tumor post-irradiation. However, such tumors are in the minority; while most tumors showed increases in hemoglobin saturation post-saturation, the percentage increase in hemoglobin saturation was modest, and hemoglobin saturation maps pre- and post- irradiation showed little-to-no contrast. It could be inferred that for E0771 tumors, at 48 hours post-irradiation, vascular remodeling is still underway and is not always sufficiently sophisticated to be the main determinant in radiation-induced reoxygenation.

It is worth noting at this juncture that oxygenation after irradiation was only measured at a single timepoint – 48 hours post-irradiation. Hu *et al.* had demonstrated that oxygenation kinetics differ between tumors.[31] Therefore, there lies the possibility that the time at which maximal reoxygenation had occurred prior to our 48 hour timepoint. It would be worthwhile to investigate this more thoroughly in future studies by obtaining data from earlier timepoints.

Some of the limitations to the imaging technique have been discussed in Palmer *et al.*, one of which being that the nanoparticles are likely to have only remained in the

superficial layers of the tumor.[3] Far more preferable would be the ability to penetrate deeper into tumor layers so that oxygenation kinetics at various spatial locations of the tumor can be quantified. A functionalized BNP that is capable of targeting tumor cells overexpressing the folate receptor is currently under development; future work can be performed using functionalized oxygen-sensing nanoparticles to improve precision in determining locations from which F/P ratios are reported.

The presented work did not monitor tumor growth in the mice, which may have important correlations with reoxygenation – these could potentially give insights to some of the observed changes in tissue oxygenation. Two irradiated mice demonstrated large decreases in both F/P ratio and Hb saturation values of the tumors, which is inconsistent with the general trends observed. Without sufficient data on specific tumor characteristics, it becomes challenging to determine how well a tumor responds to irradiation, and how its response influences or is influenced by reoxygenation. Hu *et al.* have demonstrated that changes in hemoglobin saturation have correlations with tumor control.[31] This correlation may also expand to changes in tumor oxygen tension. Tumor measurements were, however, not feasible in the current study – at the current timescale, it would be challenging to accurately measure changes in tumor size through the use of calipers. This problem is also compounded by the fact that tumors studied in dorsal window chambers are fairly small.

The present study investigated changes in mean F/P ratio and mean Hb saturation after irradiation. However, it may be worthwhile in future studies to compare pre- and post-irradiation maps pixel-by-pixel, so as to determine how different areas of a tumor respond differently to radiation. Palmer *et al.* had previously shown in a mouse tumor that there is variable temporal fluctuations in pO_2 across different regions of a tumor.[3] Determining how this translates into differing radiation responses in terms of pO_2 could be a meaningful undertaking in future studies.

Our studies have successfully validated the feasibility of fluorescent imaging of dual-emissive oxygen-sensing BNPs and hemoglobin saturation imaging in investigating oxygen kinetics in the tumor microenvironment, post-irradiation. While the current work is performed on E0771 tumors at a specific time-scale (48 hours), its ability to produce quantifiable results demonstrates its usability in a wider body of work relevant to oxygen sensing in tumors. Palmer *et al*. have previously successfully used the same method for serial imaging of the state of oxygenation in mice tumors over the course of 1 hour.[3] As such, it would also be feasible to investigate reoxygenation at a much shorter time scale. In doing so, the mechanics of reoxygenation post-irradiation can be quantified over different time periods in the reoxygenation process. This would enable a more precise understanding of both hypoxia and the reoxygenation process post-treatment, opening up possibilities for research into improved therapeutic techniques that account for oxygenation changes in tumors.

3 Investigating Uptake of Folic Acid-Conjugated Boron Nanoparticles

3.1 Introduction

In the previous chapter, we have established that dual-emissive boron nanoparticles are capable of oxygen tension quantification after irradiation. The results had also demonstrated reoxygenation in E0771 murine tumors. However, one of the limitations in the presented work was that the boron nanoparticles were not targeted to the tumor cells, and had been injected into the tumor under the glass cover of the window chamber. As such, the boron nanoparticles may only be present in the superficial layers of the tumor. In view of this limitation, we sought to target boron nanoparticles to cancer cells that overexpress the folate receptor, FOLR1.

The aim of the project presented in this chapter is to determine if fluorescent folic acid-conjugated boron nanoparticles (BNP+FA; boron nanoparticles without folic acid will be henceforth referred to as BNP-FA) can successfully target FOLR1-expressing cancer cell lines. The ability to target particular cells is critical in enhancing the efficacy of imaging and therapeutic applications of the nanoparticles. In this case, targeting BNPs to FOLR1-expressing cancer cell lines ensures that future studies using these BNPs will enable quantification of pO_2 in FOLR1-expressing tumors but not surrounding normal tissue. It also serves to potentially provide enhanced uptake of BNPs into the tumor

tissue for improved signal-to-background, as well as a means of assessing the magnitude and distribution of FOLR1 expression.

This project consisted of capturing and analyzing fluorescent images of FOLR1-expressing cells that had been incubated with BNP+/-FA solutions. Uptake of nanoparticles by the cells will be demonstrated by fluorescence in these cells. This project used the MDA-MB-231 cell line, which is a human-derived epithelial adenocarcinoma cell line.[63] It is a triple negative breast cancer cell line that is known to be highly aggressive and invasive.[64] We hypothesized that there will be significantly increased uptake of BNP+FA as compared to BNP-FA, which will be demonstrated by a higher fluorescent intensity per cell in fluorescent microscopy images, as well as a higher number of fluorescing cells in the fluorescent images. A Western blot was also performed to verify FOLR1 protein expression. After correcting for background signal from autofluorescence, two-way ANOVAs were performed on the fluorescence data obtained to determine statistical significances. The results showed that there was a statistically significant higher percentage of cells that experienced uptake of BNP+FA, as compared to uptake of BNP-FA. There was also a significant difference between the fluorescence intensity of cells incubated in BNP+FA and that of cells incubated in BNP-FA.

3.2 Methods

3.2.1 Boron Nanoparticle Characterization

For both BNP+FA and BNP-FA, fluorescence spectra were obtained from a SpectraMax® M5 spectrophotometer across a range of temperatures to establish temperature dependence. Each nanoparticle solution was made up to 20% concentration in separate cuvettes. $200\mu l$ of each nanoparticle stock solution was diluted in $800\mu l$ of deionized water, totaling $1ml$ of nanoparticle solution. The nanoparticle solutions were vortexed for a few seconds to ensure proper mixing. To test for temperature dependence, spectral readings were obtained at 22°C, 25°C, 28°C, 31°C, 34°C, 37°C, and 40°C. The excitation wavelength used was 390nm, and emission wavelengths at which signal was obtained ranged from 390nm to 590nm in 5nm intervals.

3.2.2 General Cell Culture

MDA-MB-231 cell lines were cultured in Gibco® phenol-red free minimum essential media (1X) (Reference No. 51200-038). Added to the media were 1% antibiotic-antimycotic, 10% heat-inactivated fetal bovine serum, 0.5% non-essential amino acids and 1% sodium pyruvate.

Cells were incubated at 37°C, 5% CO_2 in a humidified environment. When passaging, the cells were first rinsed with sterile 1X phosphate-buffered saline (PBS). An appropriate volume of 0.25% Trypsin-EDTA (3ml when culturing in T75 flasks) was

then added, and the cells were incubated for 5 minutes. Thereafter, the trypsinized cells were neutralized with double the amount of cell media in a centrifuge tube and centrifuged at 180G for 4 minutes. The supernatant was discarded, and the cell pellet was resuspended in fresh media before being cultured in new flasks or dishes. The cells were split with a 1:10 ratio weekly.

3.2.3 BNP+/-FA Uptake Experiment

Pilot studies were first conducted using protocols common to nanoparticle uptake studies to determine optimal BNP+/-FA concentrations and incubation times.[36,65] These pilot studies, however, revealed that the BNP+/-FA tended to adhere to the bottom of a 96-well black plate. Hence, modifications to the original protocol were made such that only nanoparticles that were within the cells would be imaged. These modifications will be discussed in detail later in the chapter.

Using the modified protocol, uptake of each type of nanoparticle was tested at 6 different concentrations: 0%, 5%, 10%, 15%, 20%, and 25%.

20 000 cells were first seeded in each well of a 24-well Greiner® clear bottom plate overnight to ensure adhesion. 150μl of BNP solutions of each concentration were then transferred to the respective wells and incubated with the cells overnight. Figure 3.1 shows the set-up of the incubation plate. Rows A and C were filled with BNP+FA solutions, and rows B and D were filled with BNP-FA solutions.

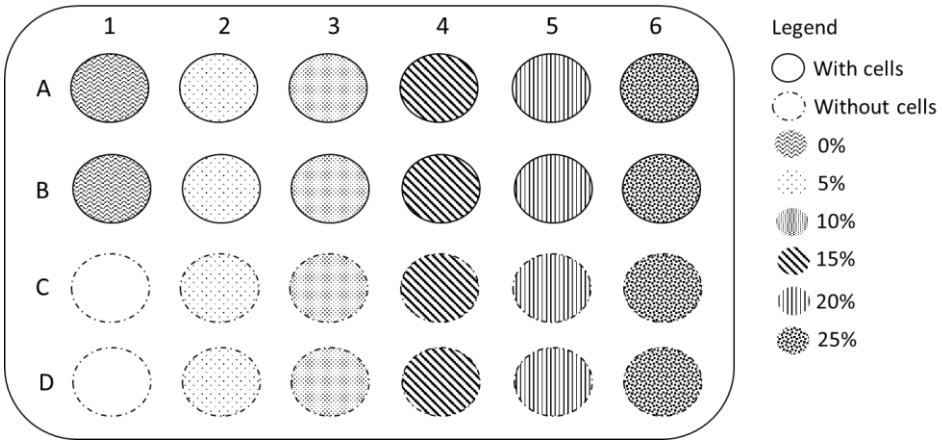

Figure 3.1: Set-Up of BNP Incubation Plate

Following incubation, wells without cells were left untouched; the emission spectra of the nanoparticles in these wells were later obtained through the SpectraMax® M5 to test for changes in fluorescence intensity. The wells with cells were washed with PBS, and the cells in these wells were trypsinized. After neutralizing the trypsin with the appropriate volumes of the respective cell media, the cells were centrifuged, and the supernatant removed. The cell pellet for each condition was then resuspended in fresh media and transferred to 3 wells of a Greiner® 96-well black plate for imaging. Figure 3.2 shows the set-up of the imaging plate.

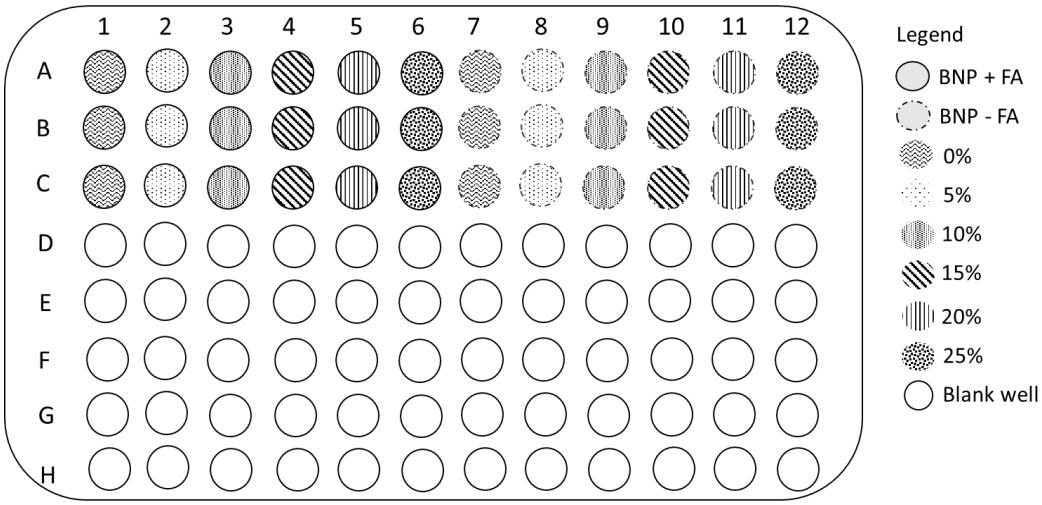

Figure 3.2: Set-Up of 96-well Black Imaging Plate

Fluorescent images of the individual wells were then obtained with a Zeiss Observer.Z1 microscope via a Hamamatsu ORCA-Flash 01 camera. The excitation and emission spectra were filtered, respectively, at 358nm and 463nm using a DAPI filter cube. Magnification was set to 20X. Brightfield images were also captured to determine the positions of the cells in each well. Emission spectra of the wells were obtained on a SpectraMax® M5 and recorded on Spectra Suite software.

ImageJ was used to analyze the images of the cells. Brightfield images were used to determine the number of cells in each image and their locations. Each cell in the corresponding brightfield image was identified as a region of interest (ROI), and an ROI mask was obtained using the *Analyze Particles* function. This ROI mask was overlaid on the fluorescence images, and the fluorescence intensities within the ROIs were measured. Figure 3.3 demonstrates this process.

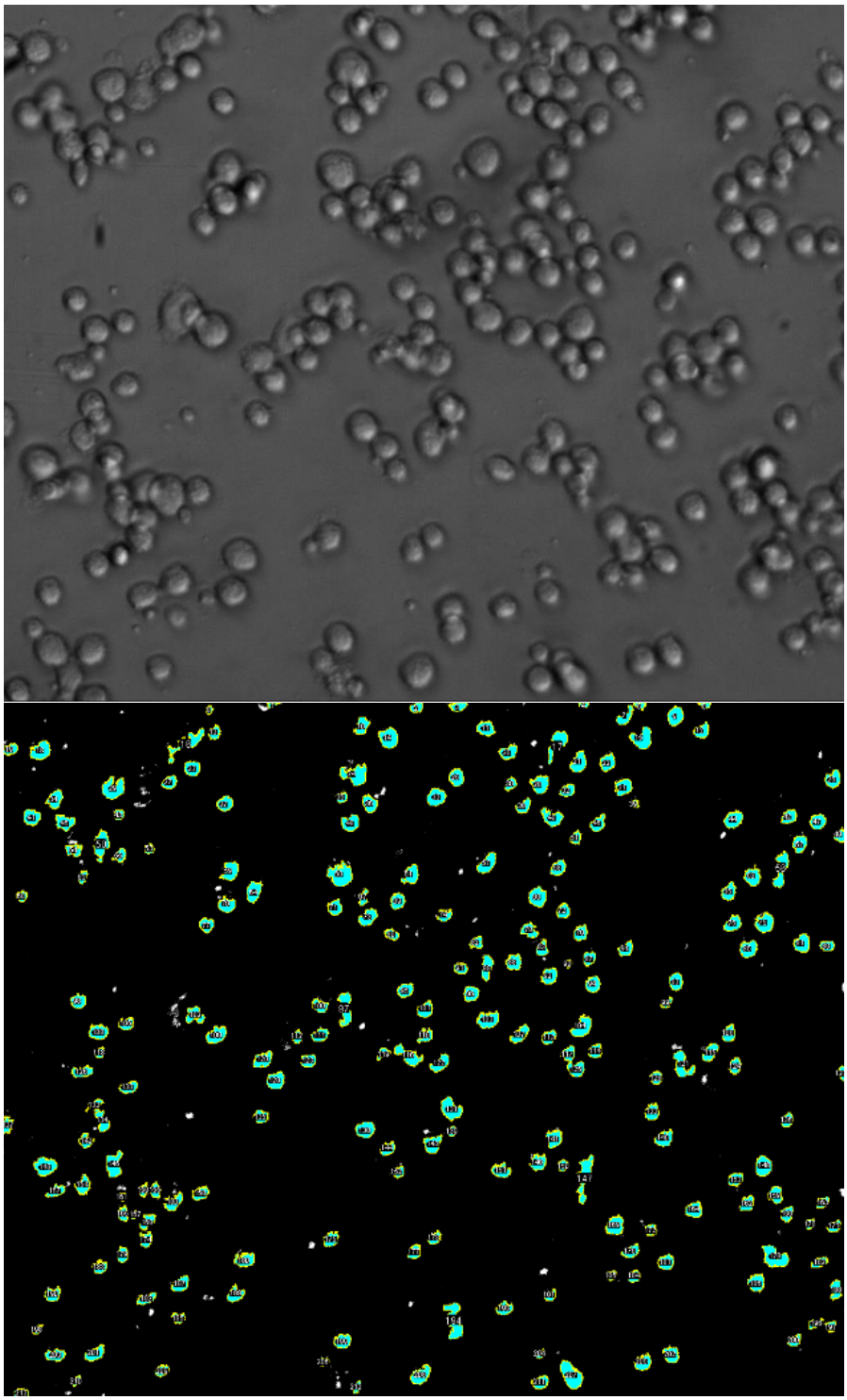

Figure 3.3: Counting Cells via the Analyze Particles function on ImageJ (Top) Raw Brightfield Image; (Bottom) ROI Mask obtained (to be applied on raw fluorescence image)

The intensity values of the images incubated only in media were averaged to obtain the average mean background signal. This mean was then subtracted from all other fluorescent images. After subtraction, a cell was considered to have fluorescence signal, and hence exhibited BNP uptake, if the intensity was more than two times above the standard deviation of the average background signal. Thereafter, a two-way ANOVA was performed on GraphPad PRISM to determine whether there was a significant difference in BNP uptake ratios between BNP+FA and BNP-FA conditions, and whether the magnitude of fluorescence intensities differed significantly between different incubation conditions.

3.2.4 Assessing FOLR1 expression: Western Blot

Previous literature presented inconclusive evidence on the abundance of folate receptor alpha (FOLR1) in MDA-MB-231 cells – Hu *et al.*'s Western blot showed rather strong signal of the FOLR1 protein in MDA-MB-231 cells, while Jain *et al.*'s and Necela *et al.'s* qPCR tests indicated weak FOLR1 mRNA expression. However, all agreed that FOLR1 was present in MDA-MB-231 cells.[27,66,67] A Western blot was performed to verify FOLR1 protein expression in the MDA-MB-231 cells that were used in this work. Cells were cultured until 100% confluent on a 35mm dish. The media was aspirated, and the cells were washed thrice with PBS. 75μl of New England Lab's 1X red loading buffer (NEB #B7703) was added to each dish. The cell dish was scraped thoroughly using cell

scrapers, and the cell lysates were pipetted into a microcentrifuge tube. The cell lysates were boiled for 7 minutes and then left to cool. After cooling, the lysates were spun down to reduce viscosity, then sonicated using a tip sonicator to shear the DNA. The lysate was then spun at maximum speed (20 000X G) again for 10 minutes to eliminate froth.

A BioRad 4x-20x Mini-PROTEAN gel was set up in a gel electrophoresis tank, and the tank was filled with PBS (1% Tween) running buffer. Actin, a housekeeping gene, was chosen as the loading control. Since it has a similar molecular weight to the FOLR1 protein (approximately 38kD), a total of 80μl of protein sample was evenly loaded into two lanes of the gel – one lane to be blocked with the primary antibody for FOLR1 and another to be blocked with the antibody for actin. After loading, the gel was run at 120V for an hour. Upon separation, the proteins were transferred to a nitrocellulose membrane using the Invitrogen Novex iBlot system. The membrane was cut into two and incubated overnight at 4°C – one half was blocked in 5% dry milk and 10$\mu g/ml$ mouse anti-human monoclonal FOLR1 antibody (R&D Systems, Minneapolis, MN, USA); the other in 5% dry milk and 1:5000 mouse anti-actin antibody (Sigma-Aldrich, St Louis, MO, USA). After blocking, the antibodies were washed thrice with PBS (1% Tween) for 20 minutes each time. The membranes were then blocked with secondary anti-mouse IgG with 680 fluor (LICOR 925-68020) at a dilution of 1:10 000 for an hour. After rinsing off the secondary antibodies thrice with PBS (1% Tween) buffer,

the membrane was imaged on a LICOR Odyssey scanner. Scans were visualized using LICOR ImageStudio lite version 4.

3.3 Results

3.3.1 Boron Nanoparticle Characterization

When the particles were first received, the emission spectra revealed that the fluorescence peak for both particles occur at approximately 420nm, with a second smaller peak at 430nm. There were also insignificant differences in fluorescence signal intensities between BNP+FA and BNP-FA. Figure 3.4 below shows the emission spectra at 37°C, which is the cell incubation temperature.

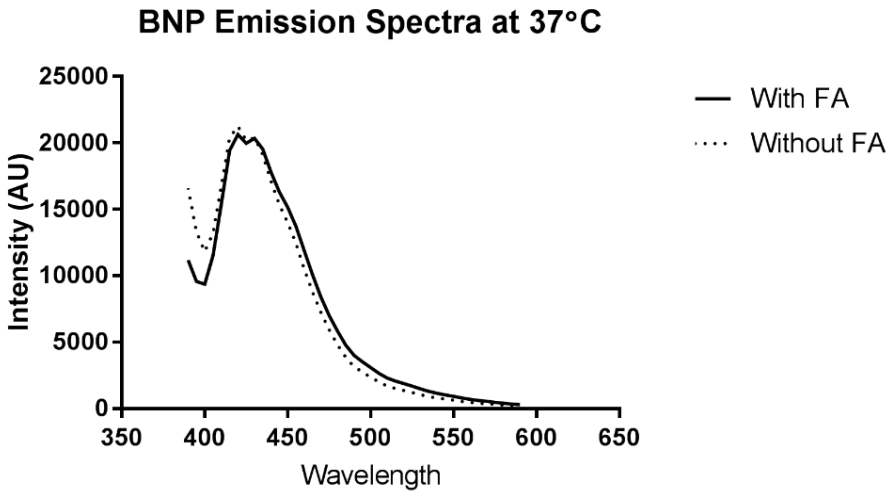

Figure 3.4: Emission Spectra of BNPs at 37°C

Fluorescence intensity decreases with increasing temperature for both types of BNPs. Figure 3.5 shows the changes in fluorescence intensity at the fluorescence peak of 420nm across a range of temperatures.

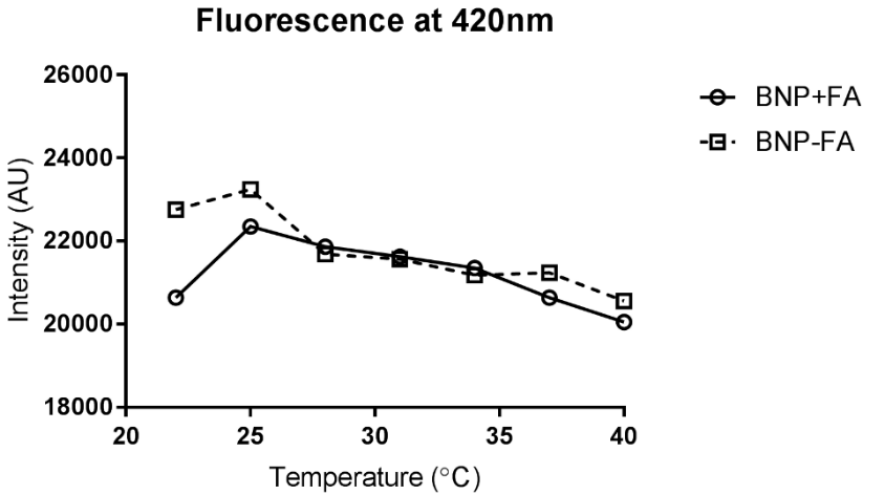

Figure 3.5: Fluorescence Intensity at a Range of Temperatures

Since there appears to be a decreasing trend in fluorescence intensity with increasing temperature, it is imperative to determine if there are significant decreases in intensity of fluorescence after incubation. This was achieved by allocating wells to be filled only with nanoparticle solution in the same incubation plate. The fluorescence spectra of these nanoparticles were recorded via the SpectraMax® M5 before and after incubation.

3.3.2 BNP+/-FA Uptake Experiment

3.3.2.1 Fluorescence of BNPs Pre- and Post- Incubation

The spectra obtained from the spectrophotometer revealed that the fluorescence intensity of both BNP+FA and BNP-FA decreased after incubation by approximately 25%. However, fluorescence was still detected, even in the 5% BNP conditions. This indicates that BNP fluorescence can still be observed after incubation at 37°C for 24 hours. Figure 3.6 shows the spectra obtained pre- and post- incubation for both BNP+FA and BNP-FA.

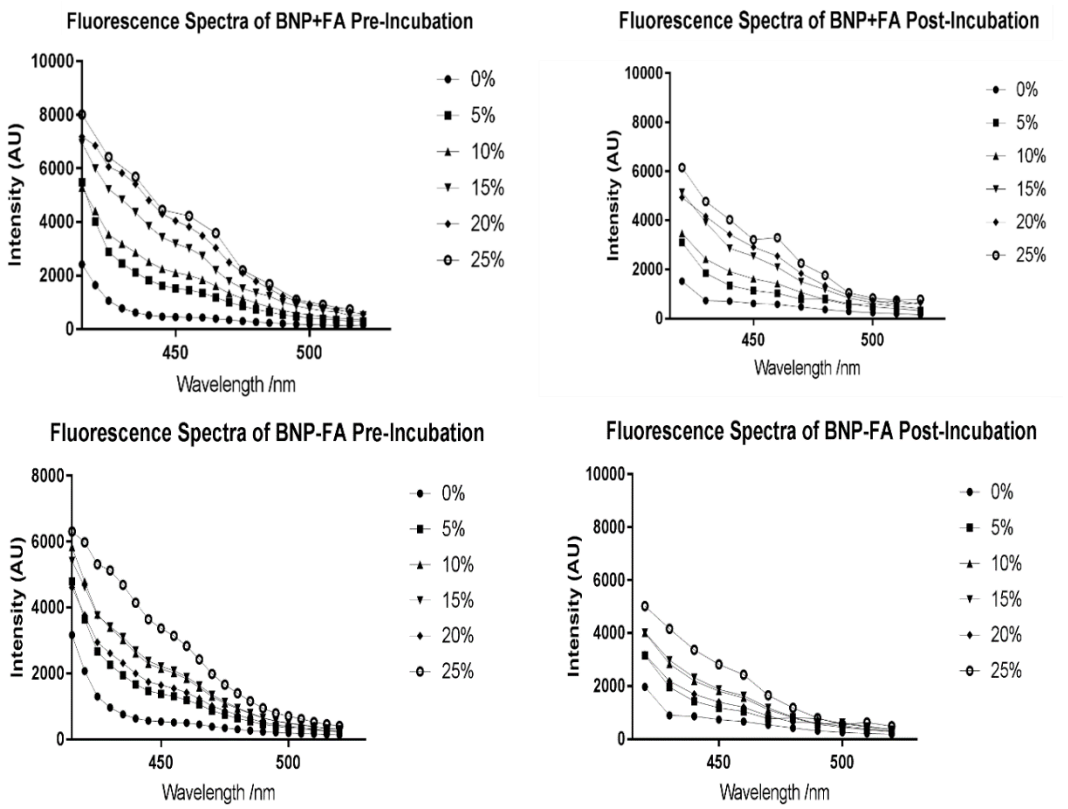

Figure 3.6: (Top) Spectra of BNP+FA, pre- and post- incubation; (Bottom) Spectra of BNP-FA, pre- and post- incubation. For both types of BNP at all concentrations, the intensities of fluorescence at 420nm decreases after 24 hours of incubation in a 37°C incubator.

3.3.2.2 Observable Fluorescence

Fluorescence was observed in cells that were subjected to incubation with BNP+FA, while little-to-no fluorescence was observed in cells subjected to incubation with BNP-FA. Figure 3.7 shows an example of the fluorescence images at a nanoparticle concentration of 25%.

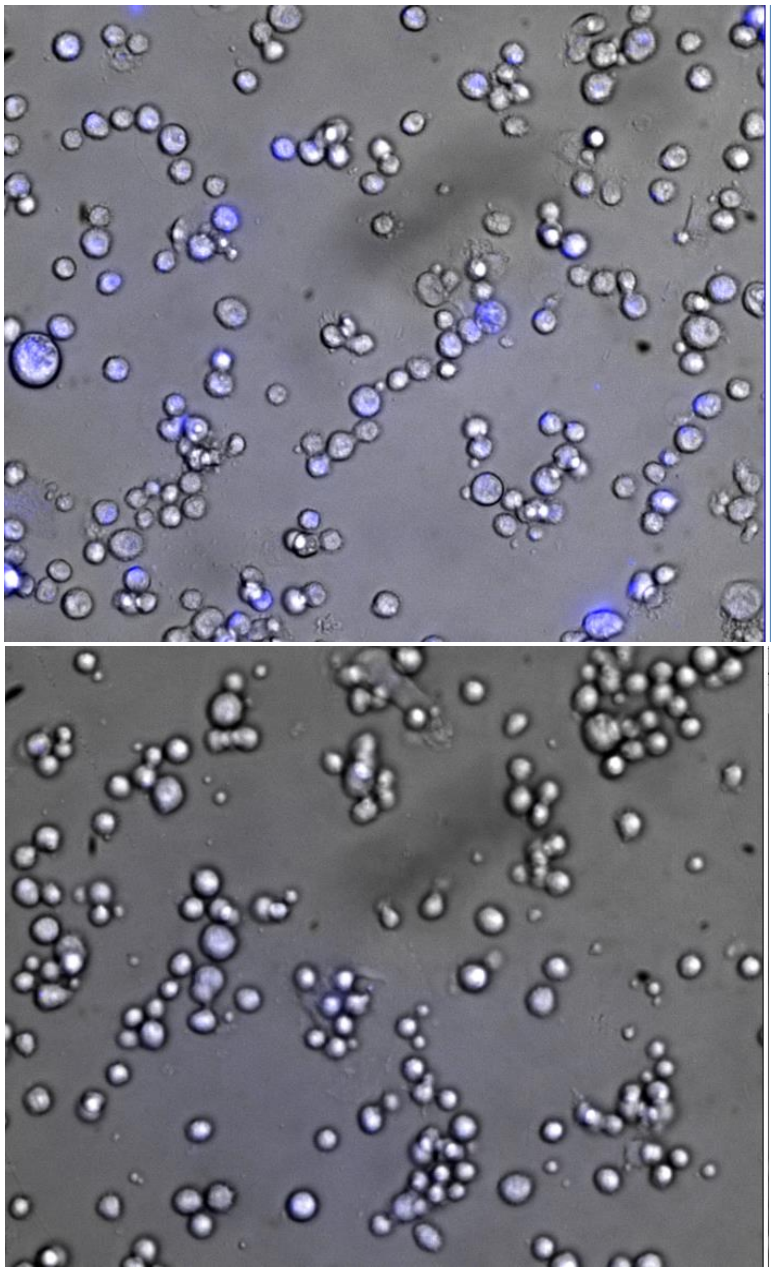

Figure 3.7: (Top) Fluorescence image of cells incubated with 25% BNP+FA; (Bottom) Fluorescence image of cells incubated with 25% BNP-FA

3.3.2.3 Uptake Ratio

Close to 100% uptake was observed for cells incubated in BNP+FA at all concentrations – that is, close to 100% of cells in the imaged wells were observed to fluoresce. In the BNP-FA conditions, uptake ratios varied between 3% to 20% for the different concentrations, with no obvious trend. Figure 3.8 displays the uptake ratios of both conditions.

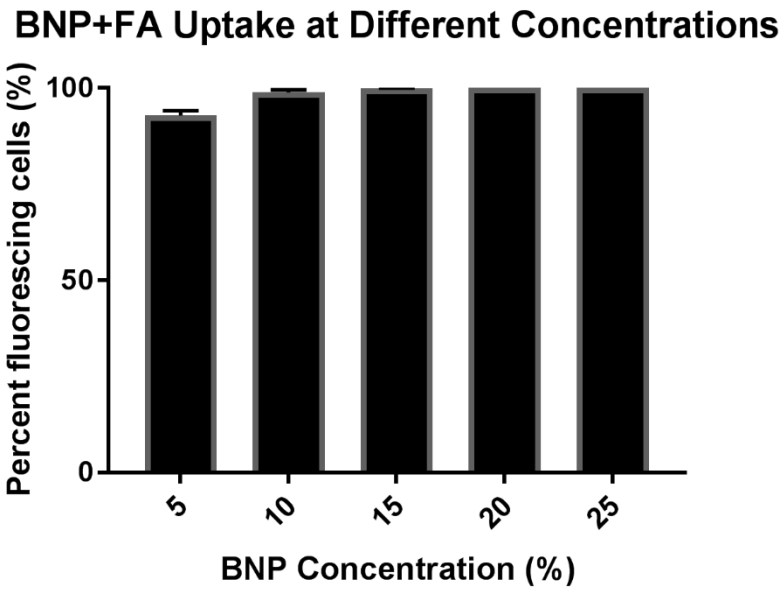

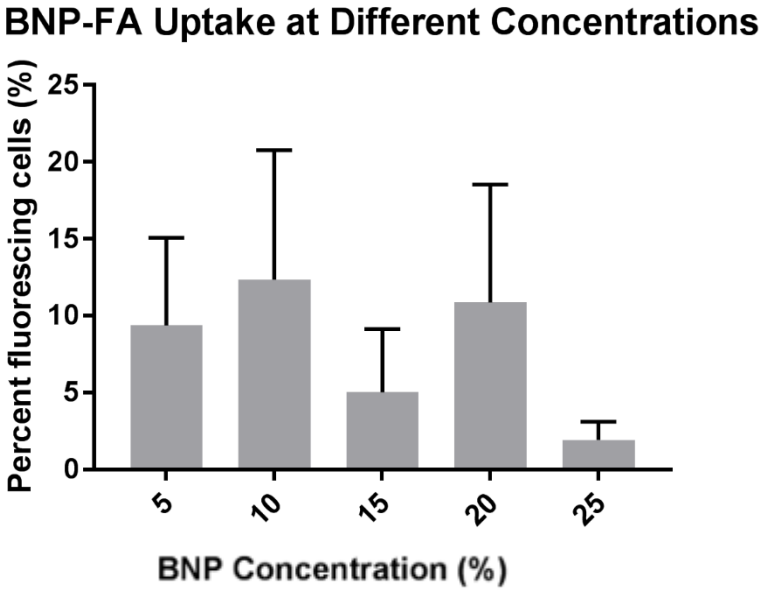

Figure 3.8: Percentage of cells experiencing BNP uptake under different concentrations of BNP incubation, with standard error shown as error bars. Close to 100% of cells imaged experienced BNP+FA uptake at all concentrations of BNP+FA, but there is a much smaller percentage of cells experiencing BNP-FA uptake. (Top) BNP+FA Uptake (Bottom) BNP-FA Uptake

As is also demonstrated by Figure 3.8, no significant differences existed between the incubation groups within each BNP type.

When comparing the uptake ratio between BNP+FA and BNP-FA at each respective concentration, significance ($p<0.0001$) exists at every concentration (Figure 3.9).

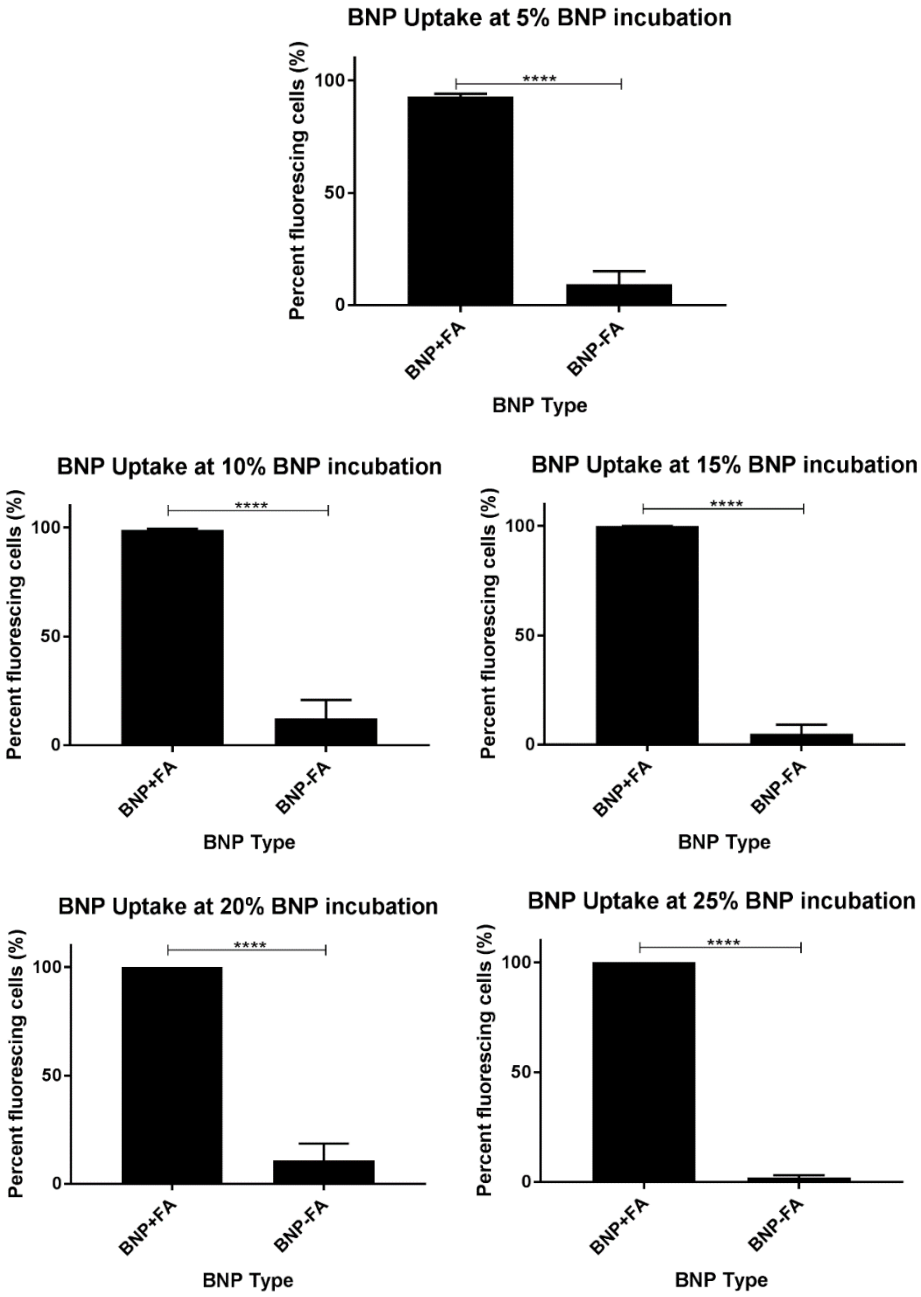

Figure 3.9 (same data as Figure 3.8): Differences in uptake ratios between BNP+FA and BNP-FA at each concentration, with error bars indicating standard error. Two-way ANOVA tests revealed significant differences ($p<0.0001$) between percent of cells experiencing BNP+FA and BNP-FA uptake at every concentration of BNP incubation.

3.3.2.4 Differences in Intensities

When considering the magnitude of fluorescence intensities, two-way ANOVA revealed statistical differences exist between cells incubated in BNP+FA and cells incubated in BNP-FA at concentrations of at least 10%. At 10% concentration, the p-value was 0.0475; at 15%, 20%, and 25% concentrations, the p-values were below 0.0001 (Figure 3.10).

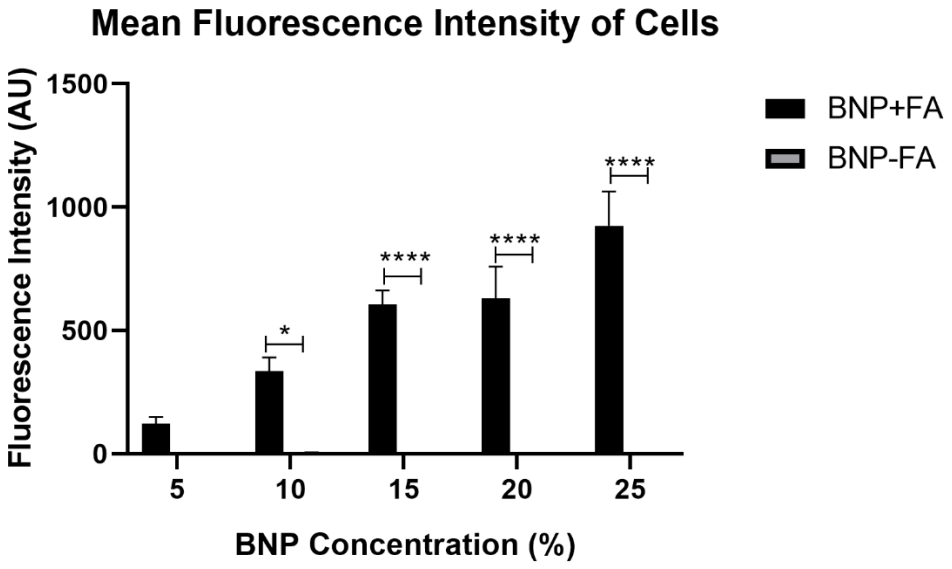

Figure 3.10: Differences in mean fluorescence intensity of all cells. The mean fluorescence intensities of cells incubated in BNP-FA are too small to be seen on a linear scale. At 5% concentration, 2-way ANOVA revealed no significant difference between the fluorescence intensity of cells incubated in BNP+FA and that of cells incubated in BNP-FA. However, at 10% BNP concentration onwards, significance ($p=0.0475$) exists between the fluorescence intensity of cells with BNP+FA incubation and that of cells with BNP-FA incubation. The difference becomes more significant ($p<0.0001$) at 15% concentration of BNP incubation and beyond.

There appeared to be an increasing trend in fluorescence intensity of the cells as concentration of BNP+FA increased; no such trend was observed for cells incubated in

BNP-FA. A linear regression was performed on the data from the cells incubated in BNP+FA, and the results are shown in Figure 3.11. The linear regression had a p-value of less than 0.0001, indicating that concentration has a statistically significant association with mean fluorescence intensity.

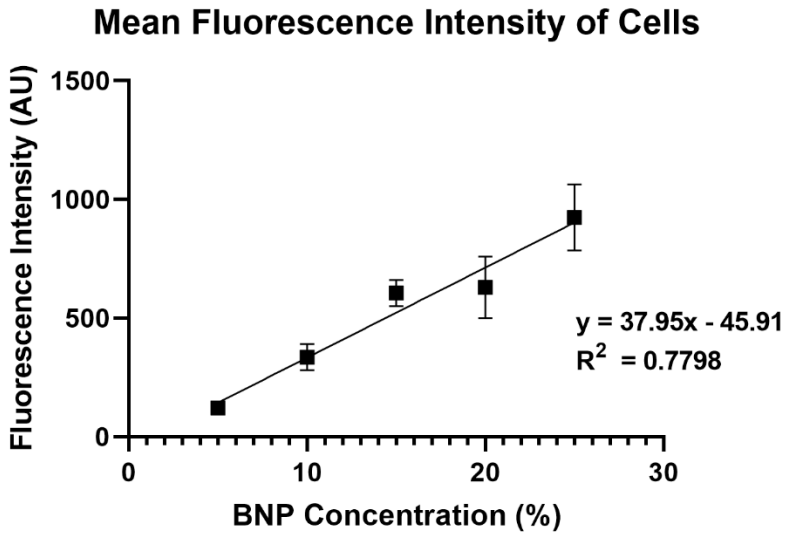

Figure 3.11: Linear Regression of Mean Fluorescence Intensities of Cells incubated in BNP+FA

3.3.3 Assessing FOLR1 Expression: Western Blot

The results of the Western blot indicated weak presence of the FOLR1 protein in MDA-MB-231 cells (Figure 3.12).

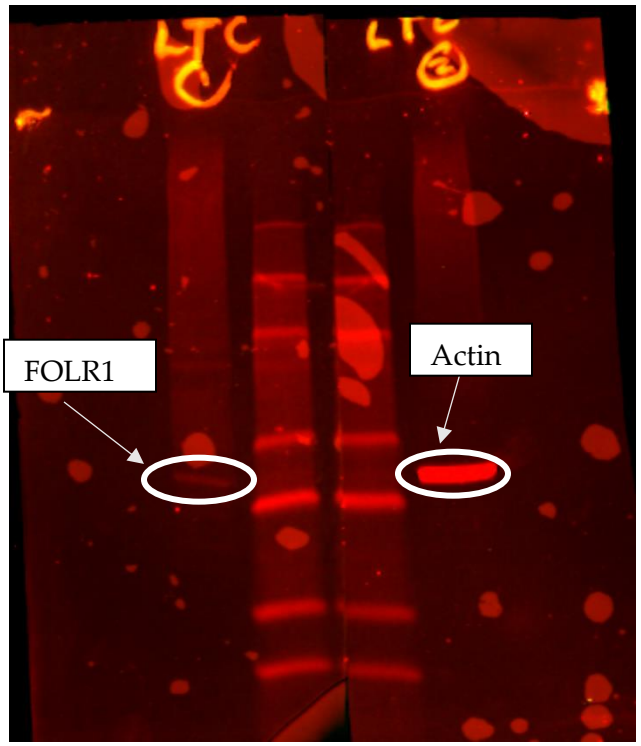

Figure 3.12: Image of blot used to determine presence of FOLR1 protein. The outermost lanes were filled with the cell lysates, while the middle two lanes consist of protein ladders.

3.4 Discussion

3.4.1 Adhesion of BNPs to 96-well Plates

The original protocol did not transfer the incubated cells from an incubation plate to an imaging plate. Instead, after incubation with the BNPs in a 96-well plate, the BNPs and cell media were aspirated, and the cells were rinsed thrice with PBS. The cells were then imaged. This is a protocol typical to nanoparticle uptake experiments in existing literature, as previously mentioned. However, in the boron nanoparticle

experiments, the wells that did not have cells also had extremely high fluorescence signal even after aspiring the BNP-mixed media and rinsing the wells with PBS. This seemed to indicate that the BNP was adhering to the plates, which was problematic – the fluorescent signal from these additional BNPs would add to the fluorescent signal obtained from directly imaging the cells in the incubation wells. To ensure that only BNPs within the cells would be imaged, additional steps were introduced to the original protocol. The main modification was the addition of a transfer step; after incubation with the BNPs, the cells were transferred to a different imaging plate. The introduction of a trypsinization and centrifugation step directly before imaging meant that the cells were not adhered to the plate at the time of imaging. This also ensured that only viable cells were imaged, since centrifugation removed dead cells.

3.4.2 Effectiveness of FA Conjugation in BNP Uptake

There is clear evidence of selective uptake of BNP+FA by the MDA-MB-231 cells. BNP concentration of the BNP+FA in the incubation media has a weak effect on the efficacy of BNP+FA targeting; nearly 100% of cells imaged exhibited fluorescence, indicating BNP+FA uptake, even at low concentrations. However, the correlation coefficient between BNP concentration and intensity of fluorescence is rather high. If we assume that fluorescence intensity is dependent on the number of BNPs present in the cell, then it appears that higher concentrations of BNP+FA in the media increases the number of particles that each cell internalizes.

It was also observed, but not quantified, that the number of viable cells that were transferred to the 96-well imaging plate decreased with increasing concentration of BNP. In general, nanoparticle studies have demonstrated that high concentrations of nanoparticles have the potential to adversely affect cell viability and/or function.[68,69] One mechanism through which high nanoparticle concentration could adversely affect cell function is via the over-production of reactive oxygen species, which results in oxidative stress.[68] However, our BNPs have thus far not shown signs of cytotoxicity in *in vivo* studies. It may be of interest to determine if there are long-term cytotoxicity effects that are correlated with BNP concentration.

Future studies could give a more robust quantification of the efficacy of folic acid conjugation in targeting FOLR1-expressing cells. The results of the Western Blot seem to indicate that there is a small amount of FOLR1 protein present on MDA-MB-231 cells. The same uptake assay could be performed on different cell lines with varying FOLR1 expression, and the amounts of FOLR1 protein present in each cell line could be quantitatively compared to determine how well the BNP+FAs were internalized.

This experiment was performed with a 24-hour incubation time, and resulted in nearly 100% of cells exhibiting BNP uptake even at low concentrations. Initially, pilot studies had been performed with a 4-hour incubation time, but results from these demonstrated little-to-no uptake of the nanoparticles. Future experiments can be performed to determine the minimum amount of incubation time needed to achieve

maximal uptake. Measurements of the minimum incubation time needed would allow better quantification of the efficiency of internalization of the BNP+FAs. A shorter incubation time, indicating higher internalization efficiency, would be ideal since fluorescence and phosphorescence intensities decrease over time; shorter incubations would ensure higher quantum yield of both luminescence processes, in turn ensuring more accurate ratiometric measurements.

Current folate receptor-targeting nanoparticles that are being investigated have reported varying incubation times that were necessary for successful internalization. Jain *et al.* reported that their folic acid functionalized nanoparticle, which has clinical applications in breast cancer diagnostics, remained on the outer membrane of MDA-MB-231 cells even after long incubation times *in vitro*.[66] The nanoparticle was more successful in targeting T-47D cells, which reportedly had a much higher expression of FOLR1.[66] In contrast, our folic acid-conjugated BNP were internalized by MDA-MB-231 cells within 24 hours, suggesting higher efficiency in the internalization process of our nanoparticles.

3.4.3 Future Prospects

A long-term aim is to use these folic acid-conjugated boron nanoparticles in both animal models and humans. To this end, the nanoparticles' ability to target FOLR1-expressing tumors *in vivo* must be assessed. Kim *et al.* have reported successful uptake of their ^{99m}Tc-labelled PEG-folate both *in vitro* and *in vivo*; similar work can be performed with our boron nanoparticles to evaluate if uptake efficiencies are changed from an *in*

vivo to an *in vitro* environment.[70] It may also be of interest to determine how long the nanoparticles remain in the tumors in an *in vivo* environment.

The folate receptor is commonly overexpressed in a variety of cancers, and is most commonly expressed in ovarian cancers.[71] While the current work focuses on breast cancers, a tangential application of the current fluorescent folate-receptor targeting nanoparticle is in imaging metastatic ovarian cancer. Pilot studies by van Dam *et al.* and Tummers *et al.* have demonstrated the clinical utility of folate receptor-targeting agents in intraoperative fluorescent imaging of ovarian cancers, while Kennedy *et al.* have shown their use in mice studies.[72–74] Our boron nanoparticle thus holds the potential to add to this growing body of literature.

Triple negative breast cancers, for which no targeted therapy currently exists, also tend to overexpress the folate receptor.[27] While normal breast epithelial cells also express folate receptors, Elnakat and Ratnam have previously shown that unlike breast tumor cells, breast epithelial cells are unable to access folate in circulation.[28] Hence, folate receptor-targeting nanoparticles like ours demonstrate potential for use in targeted therapies for triple negative breast cancer. As an example, chemotherapy drugs can be attached to nanoparticles targeted to tumors in order to minimize toxicity to normal tissue and maximize tumor kill. Since overexpression of folate receptors is also correlated with poor patient outcome, it may also be of clinical interest to target therapies to cancer cells with folate receptor overexpression.[26,75] Cheung *et al.'s* review in

2016 reported clinical trials of folate-tubulysin, which have therapeutic applications in triple negative breast cancers – as at the time of writing, these clinical trials are still ongoing.[71] Paulmurugan *et al*. have also reported on folate-targeting polymeric micillelar nanocarriers for drug delivery of the drug orlistat.[76] However, there has been few reported developments of folate-targeting nanoparticles with both imaging and therapeutic capabilities. If oxygen-sensing capabilities are added to our folate-targeting boron nanoparticles, further addition of therapeutic functions could potentially enable real-time tumor dynamics visualization and therapeutic response. Further work is warranted to determine how well anti-cancer drugs could potentially be added to our boron nanoparticle for such applications.

4 Future Implications

The objectives of this thesis include both technological and biological ones. On the biological front, the work presented in Chapter 2 sought to more clearly elucidate the mechanisms of reoxygenation some time post-irradiation. Two technological objectives were also outlined and fulfilled in Chapters 2 and 3: in chapter 2, the use of dual-emissive oxygen-sensing boron nanoparticles to characterize oxygen tension in the tumor microenvironment was validated; in chapter 3, the targeting ability of folic acid-conjugated boron nanoparticles to folate receptor-overexpressing breast cancer cells was demonstrated. The success in meeting these objectives has implications on studies henceforth. The direct implications have been discussed briefly in the respective chapters; this chapter elaborates on these next steps, and also presents a broader perspective that considers the results from both pieces of work.

Having successfully validated the feasibility of using boron nanoparticles to quantify oxygen tension in irradiated tumors, an immediate next step would be to use these nanoparticles to investigate reoxygenation processes over different time scales, and under different treatment conditions. Diaz *et al.* have used hemoglobin saturation quantification to investigate reoxygenation in fractionated regimes that mimic clinical treatment plans; it may be worthwhile to validate these results using our boron nanoparticles which offer direct quantification of tumor oxygen tension, and would thus

more accurately delineate reoxygenation processes.[52] Through knowledge of these processes, better informed decisions can be made when considering fractionation schemes in radiotherapy in the clinic.

The addition of folate receptor targeting abilities to nanoparticles opens up the possibility of targeting a variety of diagnostic and therapeutic functions to folate receptor-overexpressing cell lines. A question that arises, here, is this: how important is the need to target cell lines that overexpress the folate receptor? The introductory chapter in this thesis addresses this to some extent. Previous literature has established that many cancer cell lines, such as ovarian cancer cell lines and triple negative breast cancer cell lines, overexpress the folate receptor.[26–28,71] Its expression in normal tissue, however, is extremely limited – most normal tissues that overexpress the folate receptor are epithelial cells with limited access to circulation, as established by Elnakat and Ratnam.[26,28] Consequently, folate receptor-targeting nanoparticles show great promise in accurately targeting cancer cells. Meier *et al*., Kim *et al*., and Song *et al.* have all leveraged this characteristic by developing folate-receptor targeting nanoparticles to distinguish between normal and breast cancer cells in a variety of imaging modalities.[36,70,77]

In many of these cancers, overexpression of folate receptor has also been correlated with a myriad of undesirable outcomes, including high and early recurrence rates as well as increased tumor proliferation.[26,27,71,78] Folate receptor-overexpression has been demonstrated to confer these malignant cancer cells with a growth advantage,

especially in low folate conditions; Jhaveri *et al*. have also since shown that reducing folate receptor expression in breast cancer cells reduces their survival rates and sensitizes them to the chemotherapy drug, doxorubicin.[28,79] These findings have had important consequences on research – there has been increasing interest in developing folate receptor-targeting nanoparticles for cancer therapeutic purposes.[33–35,38,71,76] As such, it is perhaps worthwhile to explore the option of adding other imaging and therapeutic capabilities to our folic acid-conjugated boron nanoparticles.

The success in meeting both of our technological objectives with the respective boron nanoparticles presents a new objective – that of combining both oxygen-sensing and folate receptor-targeting capabilities in a single nanoparticle. The importance of targeting nanoparticles to tumors cannot be overstated, but that is only a secondary objective; the primary rationale for designing tumor-targeting nanoparticles is so that these nanoparticles can perform other diagnostic or therapeutic operations more effectively. Therefore, given that we have successfully validated the feasibility of using our dual-emissive nanoparticles for oxygen sensing operations, the natural step to take would be to enhance these oxygen-sensing nanoparticles' operative effectiveness by introducing folate receptor-targeting capabilities. These nanoparticles can then be used for investigation of oxygenation processes in tumors that overexpress the folate receptor, such as the majority of triple negative breast cancers.

Triple negative breast cancer cell lines have been shown to overexpress HIF-1α, which is correlated with poor patient prognosis.[27,80,81] HIF-1α has traditionally been understood to be stabilized by hypoxic conditions. However, in the case of triple negative cell lines, HIF-1α appears to be stabilized even when conditions are nonhypoxic. This suggests that there are other mechanisms in place that regulate HIF-1α stabilization.[80] Moeller *et al*. have previously reported that irradiation led to an increase in HIF-1α activity through the reoxygenation process.[82] It is thus of interest to determine the extent to which reoxygenation in irradiated triple negative cells promote HIF-1α stabilization and consequently worsen tumor progression. This may also provide additional insight into the utility of radiotherapy in triple breast negative cancers. Additionally, hypoxia has been correlated with increased chemoresistance, which is the main therapy of choice for triple negative breast cancers.[24] It is thus of clinical interest to quantify hypoxia in these cancers so as to better understand how current therapies can be optimized for improved patient prognosis.

Given all these, a potential application of an oxygen-sensing folate receptor-targeting nanoparticle would be to characterize the oxygenation state of the tumor microenvironment post-treatment in triple negative breast cancers. This would lend further insight into the relations between HIF-1α expression, oxygen concentration, and their responses to current treatment options in triple negative breast cancers. Knowledge of the mechanisms that promote or hinder tumor growth in these tumor environments

would advance research into more targeted therapies, which are currently lacking for triple negative breast cancers.[27]

5 Conclusion

This work has presented a number of advancements in boron nanoparticle technology for biomedical applications. First, it has validated the use of fluorescence imaging of dual-emissive boron nanoparticles in conjunction with hyperspectral imaging to quantitatively characterize the oxygen concentration of an irradiated tumor microenvironment *in vivo*. The results from this section also verified radiation-induced reoxygenation in E0771 tumors on a 48-hour time scale. In doing so, the potential for these imaging techniques to more clearly elucidate reoxygenation kinetics has been demonstrated.

Second, this work has shown the successful internalization of folic acid-conjugated boron nanoparticles in cancer cells *in vitro*. This success has important consequences on forthcoming oxygen-sensing boron nanoparticle technology: functionalized oxygen-sensing boron nanoparticles can be used in intracellular oxygen-sensing operations, and could potentially reduce signal-to-noise ratios, thus improving current BNP imaging sensitivities.

References

1. Rajendran, J. G. & Krohn, K. A. Imaging hypoxia and angiogenesis in tumors. *Radiologic Clinics of North America* 43, 169–187 (2005).

2. Matsumoto, S., Yasui, H., Mitchell, J. B. & Krishna, M. C. Imaging Cycling Tumor Hypoxia. *Cancer Res* 70, 10019–10023 (2010).

3. Palmer, G. M. *et al.* Optical imaging of tumor hypoxia dynamics. *J Biomed Opt* 15, 066021 (2010).

4. Dewhirst, M. W. Relationships between Cycling Hypoxia, HIF-1, Angiogenesis and Oxidative Stress. *Radiation Research* 172, 653–665 (2009).

5. Dewhirst, M. W., Cao, Y. & Moeller, B. Cycling hypoxia and free radicals regulate angiogenesis and radiotherapy response. *Nat Rev Cancer* 8, 425–437 (2008).

6. Harris, A. L. Hypoxia — a key regulatory factor in tumour growth. *Nature Reviews Cancer* 2, 38–47 (2002).

7. Gillies, R. J., Brown, J. S., Anderson, A. R. A. & Gatenby, R. A. Eco-evolutionary causes and consequences of temporal changes in intratumoural blood flow. *Nature Reviews Cancer* 18, 576–585 (2018).

8. Lou, W. *et al.* MicroRNAs in cancer metastasis and angiogenesis. *Oncotarget* 8, 115787–115802 (2017).

9. Michiels, C., Tellier, C. & Feron, O. Cycling hypoxia: A key feature of the tumor microenvironment. *Biochimica et Biophysica Acta (BBA) - Reviews on Cancer* 1866, 76–86 (2016).

10. Groebe, K. & Vaupel, P. Evaluation of oxygen diffusion distances in human breast cancer xenografts using tumor-specific in vivo data: role of various mechanisms in the development of tumor hypoxia. *Int. J. Radiat. Oncol. Biol. Phys.* 15, 691–697 (1988).

11. Rockwell, S., Dobrucki, I. T., Kim, E. Y., Marrison, S. T. & Vu, V. T. Hypoxia and radiation therapy: Past history, ongoing research, and future promise. *Curr Mol Med* 9, 442–458 (2009).

12. Kallman, R. & Bleehen, N. Post-irradiation cyclic radio-sensitivity changes in tumors and normal tissues. in *Proceedings of the Symposium on Dose Rate in Mammalian Radiobiology* 20.1-20.23 (Technical Information Service, 1968).

13. Rudat, V. *et al.* Predictive value of the tumor oxygenation by means of pO2 histography in patients with advanced head and neck cancer. *Strahlenther Onkol* 177, 462–468 (2001).

14. Gray, L. H., Conger, A. D., Ebert, M., Hornsey, S. & Scott, O. C. The concentration of oxygen dissolved in tissues at the time of irradiation as a factor in radiotherapy. *Br J Radiol* 26, 638–648 (1953).

15. Moeller, B. J., Richardson, R. A. & Dewhirst, M. W. Hypoxia and radiotherapy: opportunities for improved outcomes in cancer treatment. *Cancer and Metastasis Reviews; Dordrecht* 26, 241–248 (2007).

16. Siegel, R. L., Miller, K. D. & Jemal, A. Cancer statistics, 2018. *CA: A Cancer Journal for Clinicians* 68, 7–30 (2018).

17. Mcguire, A., Brown, J. A., L & Kerin, M. J. Metastatic breast cancer: the potential of miRNA for diagnosis and treatment monitoring. *Cancer and Metastasis Reviews; Dordrecht* 34, 145–155 (2015).

18. Gilkes, D. M. & Semenza, G. L. Role of hypoxia-inducible factors in breast cancer metastasis. *Future Oncol* 9, 1623–1636 (2013).

19. Kast, K. *et al.* Impact of breast cancer subtypes and patterns of metastasis on outcome. *Breast Cancer Research and Treatment* 150, 621+ (2015).

20. Fallahpour, S., Navaneelan, T., De, P. & Borgo, A. Breast cancer survival by molecular subtype: a population-based analysis of cancer registry data. *CMAJ Open* 5, E734–E739 (2017).

21. Höckel, M. *et al.* Association between Tumor Hypoxia and Malignant Progression in Advanced Cancer of the Uterine Cervix. *Cancer Res* 56, 4509–4515 (1996).

22. Nakamiya, N. *et al.* Clinicopathological and prognostic impact of imaging of breast cancer angiogenesis and hypoxia using diffuse optical spectroscopy. *Cancer Science* 105, 833–839 (2014).

23. Brizel, D. M., Sibley, G. S., Prosnitz, L. R., Scher, R. L. & Dewhirst, M. W. Tumor hypoxia adversely affects the prognosis of carcinoma of the head and neck. *International Journal of Radiation Oncology*Biology*Physics* 38, 285–289 (1997).

24. O'Reilly, E. A. *et al.* The fate of chemoresistance in triple negative breast cancer (TNBC). *BBA Clinical* 3, 257–275 (2015).

25. Kassam, F. *et al.* Survival Outcomes for Patients with Metastatic Triple-Negative Breast Cancer: Implications for Clinical Practice and Trial Design. *Clinical Breast Cancer* 9, 29–33 (2009).

26. O'Shannessy, D. J., Somers, E. B., Maltzman, J., Smale, R. & Fu, Y.-S. Folate receptor alpha (FRA) expression in breast cancer: identification of a new molecular subtype and association with triple negative disease. *Springerplus* 1, (2012).

27. Necela, B. M. *et al.* Folate Receptor-α (FOLR1) Expression and Function in Triple Negative Tumors. *PLoS One* 10, e0122209 (2015).

28. Elnakat, H. & Ratnam, M. Distribution, functionality and gene regulation of folate receptor isoforms: implications in targeted therapy. *Advanced Drug Delivery Reviews* 56, 1067–1084 (2004).

29. Roussakis, E., Li, Z., Nichols, A. J. & Evans, C. L. Oxygen-Sensing Methods in Biomedicine from the Macroscale to the Microscale. *Angewandte Chemie International Edition* 54, 8340–8362 (2015).

30. Rickard, A. G., Palmer, G. M. & Dewhirst, M. W. Clinical and Pre-clinical Methods for Quantifying Tumor Hypoxia.pdf. (2018).

31. Hu, F. *et al.* Oxygen and Perfusion Kinetics in Response to Fractionated Radiation Therapy in FaDu Head and Neck Cancer Xenografts Are Related to Treatment Outcome. *International Journal of Radiation Oncology*Biology*Physics* 96, 462–469 (2016).

32. Zhang, G., Palmer, G. M., Dewhirst, M. W. & Fraser, C. L. A dual-emissive-materials design concept enables tumour hypoxia imaging. *Nat Mater* 8, 747–751 (2009).

33. Sudimack, J. & Lee, R. J. Targeted drug delivery via the folate receptor. *Advanced Drug Delivery Reviews* 41, 147–162 (2000).

34. Zwicke, G. L., Mansoori, G. A. & Jeffery, C. J. Utilizing the folate receptor for active targeting of cancer nanotherapeutics. *Nano Rev* 3, 18496 (2012).

35. Paulos, C. M., Turk, M. J., Breur, G. J. & Low, P. S. Folate receptor-mediated targeting of therapeutic and imaging agents to activated macrophages in rheumatoid arthritis. *Advanced Drug Delivery Reviews* 56, 1205–1217 (2004).

36. Song, Y., Shi, W., Chen, W., Li, X. & Ma, H. Fluorescent carbon nanodots conjugated with folic acid for distinguishing folate -receptor-positive cancer cells from normal cells. *Journal of Materials Chemistry* 22, 12568–12573 (2012).

37. Jin, C. S., Cui, L., Wang, F., Chen, J. & Zheng, G. Targeting-Triggered Porphysome Nanostructure Disruption for Activatable Photodynamic Therapy. *Advanced Healthcare Materials* 3, 1240–1249 (2014).

38. Kato, T. *et al.* Nanoparticle targeted folate receptor 1-enhanced photodynamic therapy for lung cancer. *Lung Cancer* 113, 59–68 (2017).

39. Abdlaty, R., Sahli, S., Hayward, J. & Fang, Q. Hyperspectral imaging: comparison of acousto-optic and liquid crystal tunable filters. in *Medical Imaging 2018: Physics of Medical Imaging* 10573, 105732P (International Society for Optics and Photonics, 2018).

40. Gat, N. Imaging spectroscopy using tunable filters: a review. in *Wavelet Applications VII* 4056, 50–65 (International Society for Optics and Photonics, 2000).

41. Aharon, O., Safrani, A., Moses, R. & Abdulhalim, I. Liquid crystal tunable filters and polarization controllers for biomedical optical imaging. in *Liquid Crystals XII* 7050, 70500P (International Society for Optics and Photonics, 2008).

42. Photometrics QV2 Datasheet. (2013).

43. Hall, E. J. & Giaccia, A. J. *Radiobiology for the radiologist*. (Wolters Kluwer Health/Lippincott Williams & Wilkins, 2012).

44. Thomlinson, R. H. Reoxygenation as a function of tumor size and histopathological type. in *Proceedings of the Carmel Conference on Time and Dose Relationships in Radiation Biology as Applied to Radiotherapy* 242–254 (National Laboratory Report, 1970).

45. Rockwell, S. & Moulder, J. E. Biological factors of importance in split-course radiotherapy. in *Optimization of Cancer Radiotherapy* (eds. Paliwal, B. R., Herbert, D. E. & Orton, C. G.) 171–182 (American Institute of Physics, 1985).

46. Hockel, M. *et al.* Association between tumor hypoxia and malignant progression in advanced cancer of the uterine cervix. *Cancer Res.* 56, 4509–4515 (1996).

47. Vujaskovic, Z. *et al.* Ultrasound guided pO 2 measurement of breast cancer reoxygenation after neoadjuvant chemotherapy and hyperthermia treatment. *International Journal of Hyperthermia* 19, 498–506 (2003).

48. Nordsmark, M. *et al.* Prognostic value of tumor oxygenation in 397 head and neck tumors after primary radiation therapy. An international multi-center study. *Radiotherapy and Oncology* 77, 18–24 (2005).

49. Palmer, G. M., Vishwanath, K. & Dewhirst, M. W. Application of Optical Imaging and Spectroscopy to Radiation Biology. *Radiat Res* 177, 365–375 (2012).

50. Sorg, B. S., Moeller, B. J., Donovan, O., Cao, Y. & Dewhirst, M. W. Hyperspectral imaging of hemoglobin saturation in tumor microvasculature and tumor hypoxia development. *JBO* 10, 044004 (2005).

51. Ueda, S. *et al. In vivo* imaging of eribulin-induced reoxygenation in advanced breast cancer patients: a comparison to bevacizumab. *British Journal of Cancer* 114, 1212–1218 (2016).

52. Diaz, P. M. *et al.* Quantitative diffuse reflectance spectroscopy of short-term changes in tumor oxygenation after radiation in a matched model of radiation resistance. *Biomed. Opt. Express, BOE* 9, 3794–3804 (2018).

53. Hirakawa, Y. *et al.* Intravital phosphorescence lifetime imaging of the renal cortex accurately measures renal hypoxia. *Kidney International* 93, 1483–1489 (2018).

54. Zhao, Y. *et al.* A platinum-porphine/poly(perfluoroether) film oxygen tension sensor for noninvasive local monitoring of cellular oxygen metabolism using phosphorescence lifetime imaging. *Sensors and Actuators B: Chemical* 269, 88–95 (2018).

55. Sugiura, K. & Stock, C. C. Studies in a tumor spectrum. I. Comparison of the action of methylbis (2-chloroethyl)amine and 3-bis(2-chloroethyl)aminomethyl-4-methoxymethyl -5-hydroxy-6-methylpyridine on the growth of a variety of mouse and rat tumors. *Cancer* 5, 382–402 (1952).

56. Ewens, A., Mihich, E. & Ehrke, M. J. Distant Metastasis from Subcutaneously Grown E0771 Medullary Breast Adenocarcinoma. *Anticancer Res* 25, 3905–3915 (2005).

57. Glass, O. K. *et al.* Differential response to exercise in claudin-low breast cancer. *Oncotarget* 8, 100989–101004 (2017).

58. Palmer, G. M. *et al. In vivo* optical molecular imaging and analysis in mice using dorsal window chamber models applied to hypoxia, vasculature and fluorescent reporters. *Nature Protocols* 6, 1355–1366 (2011).

59. DeRosa, C. A. *et al.* Oxygen Sensing Difluoroboron β-Diketonate Polylactide Materials with Tunable Dynamic Ranges for Wound Imaging. *ACS Sens.* 1, 1366–1373 (2016).

60. DeRosa, C. A. *et al.* Oxygen Sensing Difluoroboron Dinaphthoylmethane Polylactide. *Macromolecules* 48, 2967–2977 (2015).

61. Shonat, R. D., Wachman, E. S., Niu, W., Koretsky, A. P. & Farkas, D. L. Near-simultaneous hemoglobin saturation and oxygen tension maps in mouse brain using an AOTF microscope. *Biophys J* 73, 1223–1231 (1997).

62. Fenton, B. M., Lord, E. M. & Paoni, S. F. Effects of Radiation on Tumor Intravascular Oxygenation, Vascular Configuration, Development of Hypoxia, and Clonogenic Survival. *Radiation Research* 155, 360–368 (2001).

63. Chavez, K. J., Garimella, S. V. & Lipkowitz, S. Triple Negative Breast Cancer Cell Lines: One Tool in the Search for Better Treatment of Triple Negative Breast Cancer. *Breast disease* 32, 35 (2010).

64. Liu, H., Zang, C., Fenner, M. H., Possinger, K. & Elstner, E. PPARgamma ligands and ATRA inhibit the invasion of human breast cancer cells in vitro. *Breast Cancer Res. Treat.* 79, 63–74 (2003).

65. Meindl, C., Öhlinger, K., Ober, J., Roblegg, E. & Fröhlich, E. Comparison of fluorescence-based methods to determine nanoparticle uptake by phagocytes and non-phagocytic cells in vitro. *Toxicology* 378, 25–36 (2017).

66. Jain, A. *et al.* Functionalized rare earth-doped nanoparticles for breast cancer nanodiagnostic using fluorescence and CT imaging. *Journal of Nanobiotechnology* 16, 26 (2018).

67. Hu, D. *et al.* Folate Receptor-Targeting Gold Nanoclusters as Fluorescence Enzyme Mimetic Nanoprobes for Tumor Molecular Colocalization Diagnosis. *Theranostics* 4, 142–153 (2014).

68. Abdal Dayem, A. *et al.* The Role of Reactive Oxygen Species (ROS) in the Biological Activities of Metallic Nanoparticles. *Int J Mol Sci* 18, 120 (2017).

69. Bahadar, H., Maqbool, F., Niaz, K. & Abdollahi, M. Toxicity of Nanoparticles and an Overview of Current Experimental Models. *Iran Biomed J* 20, 1–11 (2016).

70. Kim, S.-L. *et al.* Folate Receptor Targeted Imaging Using Poly (ethylene glycol)-folate: In Vitro and In Vivo Studies. *J Korean Med Sci* 22, 405–411 (2007).

71. Cheung, A. *et al.* Targeting folate receptor alpha for cancer treatment. *Oncotarget* 7, 52553–52574 (2016).

72. van Dam, G. M. *et al.* Intraoperative tumor-specific fluorescence imaging in ovarian cancer by folate receptor-α targeting: first in-human results. *Nature Medicine* 17, 1315–1319 (2011).

73. Tummers, Q. R. J. G. *et al.* Intraoperative imaging of folate receptor alpha positive ovarian and breast cancer using the tumor specific agent EC17. *Oncotarget* 7, 32144–32155 (2016).

74. Kennedy, M. D., Jallad, K. N., Thompson, D. H., Ben-Amotz, D. & Low, P. S. Optical imaging of metastatic tumors using a folate-targeted fluorescent probe. *JBO* 8, 636–642 (2003).

75. Ginter, P. S. *et al.* Folate Receptor Alpha Expression Is Associated With Increased Risk of Recurrence in Triple-negative Breast Cancer. *Clinical Breast Cancer* 17, 544–549 (2017).

76. Paulmurugan, R. *et al.* Folate Receptor–Targeted Polymeric Micellar Nanocarriers for Delivery of Orlistat as a Repurposed Drug against Triple-Negative Breast Cancer. *Mol Cancer Ther* 15, 221–231 (2016).

77. Meier, R. *et al.* Breast Cancers: MR Imaging of Folate-Receptor Expression with the Folate-Specific Nanoparticle P1133. *Radiology* 255, 527–535 (2010).

78. Hartmann, L. C. *et al.* Folate receptor overexpression is associated with poor outcome in breast cancer. *International Journal of Cancer* 121, 938–942 (2007).

79. Jhaveri, M. S., Rait, A. S., Chung, K.-N., Trepel, J. B. & Chang, E. H. Antisense oligonucleotides targeted to the human α folate receptor inhibit breast cancer cell growth and sensitize the cells to doxorubicin treatment. *Mol Cancer Ther* 3, 1505–1512 (2004).

80. Piccolo, S., Enzo, E. & Montagner, M. p63, Sharp1, and HIFs: Master Regulators of Metastasis in Triple-Negative Breast Cancer. *Cancer Res* 73, 4978–4981 (2013).

81. Semenza, G. L. The hypoxic tumor microenvironment: A driving force for breast cancer progression. *Biochimica et Biophysica Acta (BBA) - Molecular Cell Research* 1863, 382–391 (2016).

82. Moeller, B. J., Cao, Y., Li, C. Y. & Dewhirst, M. W. Radiation activates HIF-1 to regulate vascular radiosensitivity in tumors: Role of reoxygenation, free radicals, and stress granules. *Cancer Cell* 5, 429–441 (2004).